UMEÅ UNIVERSITY

Characterization and Improvement of Light-emitting Electrochemical Cells

Xiaoying Zhang

Department of Physics
Umeå 2025

Dissertation for PhD
ISBN: 978-91-8070-615-5 (print)
ISBN: 978-91-8070-616-2 (pdf)
Cover: Simulated outcoupling efficiency
Electronic version available at: http://umu.diva-portal.org/
Printed by: Scandinavian Print Group
Umeå, Sweden 2025

“两岸猿声啼不住，轻舟已过万重山”

——（唐）李白

Table of Contents

Abstract

The light-emitting electrochemical cell (LEC) is an emerging electroluminescent technology, which is attractive since it can deliver bright area emission at low voltage from thin and flexible devices that can be cost- and energy-efficiently fabricated by scalable printing techniques. This opens up for applications where current light emitting diode (LED) and organic light emitting diode (OLED) technologies fall short, primarily in terms of cost, sustainability and form factor. Many projected LEC applications are portable (and powered by an integrated energy storage device or by integrated wireless energy harvesting) in the realm of, for instance, MedTech, packaging, signage, security and wearables, where the available input energy is limited. Thus, achieving a high brightness at high emission efficiency, i.e. the efficiency at which the device converts electric energy to emitted light from the device structure, is critical. However, this requires a detailed understanding of the complex operational mechanism of the LEC.

When the LEC is electrically powered, the mobile ions in the active material reorganize *in situ* to form injection-enabling electric double layers followed by electrochemical p- and n-type doping and the formation of a p-n junction region. The emission zone (EZ), located in the p-n junction region where the injected electrons and holes meet and light is generated, is dynamic in the LEC due to the *in situ* electrochemical doping. This complicates the analysis of the device performance since the EZ position strongly influences the outcoupling efficiency of the light generated in the p-n junction and since the EZ width plays an important role in the internal quenching mechanisms of the LEC.

In this thesis, we present a characterization method for the measurement of the dynamic EZ in an LEC, and we add to the understanding of how an efficient LEC should be designed. The EZ position is determined with the aid of the optical microcavity effect by fitting simulated to measured angle-resolved electroluminescence spectra. By using this method, we could show that the EZ position can be shifted from close to the anode towards the center of the active material in a common LEC through the inclusion of an appropriate additive into the active material, which is very attractive since it resulted in a 60 % improvement of the emission efficiency. Secondly, we combined this method with so-called “efficiency roll-off” measurements (i.e. the drop in emission efficiency with increasing current density) to derive the internal loss factors. Specifically, by quantifying the change of the light outcoupling efficiency with the

extracted shift of EZ position, we could identify and quantify the losses due to exciton quenching. We find that the efficiency roll-off in common singlet-exciton emitting LECs is mainly due to the singlet-exciton:polaron quenching (with the polarons being the electrons and holes in the organic semiconductor). Finally, we improved the EZ measurement method by considering the doping-dependent refractive index in the optical model, by enhancing the measured emission spectra intensity at large angles by using a half-cylinder lens, and by removing the influence from the emitter's anisotropy with a polarizer. With this improved method, the EZ width can also be extracted, and we find that the EZ width decreases during the initial operation and that the EZ width at steady-state is ~20 % of the thickness of the active material for a common LEC device. In summary, the findings presented in this thesis contribute to a deeper understanding of the complex LEC doping structure, thus paving the way for brighter and more efficient LECs for practical applications.

Sammanfattning

En ljusemitterande elektrokemisk cell (LEC) är en ny typ av ljusemissionsteknologi som är attraktiv eftersom den kan leverera icke-bländande ljus vid låg spänning från tunna och flexibla filmer och tillverkas kostnads- och energieffektivt med olika skalbara tryckmetoder. Detta öppnar upp för tillämpningar där dagens ljusemitterade dioder (LED) och organiska ljusemitterade dioder (OLED) faller kort, främst vad gäller kostnad, hållbarhet och formfaktor. Många potentiella LEC-tillämpningar är portabla (och drivna av en energilagringskomponent som ett batteri eller genom integrerad trådlös energiutvinning), och ett antal tillämpningsexempel finns inom medicinteknik, förpackningar, annonsering, säkerhetstryck och ”wearables”, där den tillgängliga tillförda energin är begränsad. I sådana tillämpningar är det därför viktigt med hög emissionseffektivitet, det vill säga den effektivitet med vilken en LEC omvandlar elektrisk energi till ljus.

När en spänning appliceras mellan LEC elektroderna börjar de mobila jonerna i det aktiva materialet migrera för att först bilda så kallade elektriska dubbel-lager som möjliggör effektiv elektron- och hål-injektion följt av elektrokemisk dopning som resulterar i skapandet av en pn-övergång. Emissionszonen (EZ), som ligger i pn-övergången där de injicerade elektronerna och hålen möts och ljus genereras, är dynamisk i en LEC på grund av den elektrokemiska dopningen. Detta komplicerar analysen av en LECs prestanda eftersom EZ-positionen starkt påverkar utkopplingseffektiviteten och eftersom EZ-bredden spelar en viktig roll i de interna konverteringsprocesserna. Det är med andra ord centralt att kunna mäta EZ positionen noggrant under driften av en LEC för att därigenom kunna designa LEC komponenter med hög emissionseffektivitet.

I denna avhandling presenterar vi en karakteriseringsmetod för att mäta den dynamiska EZ hos en LEC, och vi bidrar med ny förståelse för hur en energieffektiv LEC ska designas. EZ-positionen bestäms med god noggrannhet genom att anpassa simulerade till uppmätta vinkelupplösta elektroluminiscensspektra och genom att utnyttja den optiska mikrokavitetseffekten. Med denna metod har vi visat att EZ-positionen i en LEC kan flyttas från nära anoden till mitten av det aktiva materialet genom att inkludera ett lämpligt additivmaterial till det aktiva materialet; vilket var attraktivt då det resulterade i en 60 % förbättring av energieffektiviteten. För det andra har vi använt denna metod för att kunna extrahera de interna förlustfaktorerna från mätningar av

”emissions-roll-off” (dvs hur emissions-effektiviteten avtar vid ökad strömdrivning). Mer specifikt, genom att bestämma hur ljusutkopplingseffektiviteten beror på den uppmätta EZ-positionen kunde vi separera och kvantifiera excitonförlusterna. Vi fann att emissions-roll-off i vanliga singlet-emitterande LEC-komponenter huvudsakligen beror på singlet-exciton:polaron-förluster (polaroner är benämningen för elektroner och hål i organiska halvledare). Slutligen så har vi utvecklat EZ-metoden genom att inkludera: det dopningsberoende brytningsindexet i den optiska modellen, en halvcylinderlins för att höja intensiteten hos emissionsspektra, och en polarisator för att eliminera eventuellt okänd inverkan av emitterar-anisotropi. Med vår förbättrade metod kan vi bestämma även EZ-bredden, och vi finner att EZ-bredden initialt minskar med tiden samt att EZ-bredden vid steady-state motsvarar ~20 % av den totala tjockleken hos det aktiva materialet för en vanlig LEC. Sammanfattningsvis bidrar resultaten som presenteras i denna avhandling till en förbättrad mätning av, och kunskap om, den komplexa dopningsstrukturen hos LEC-komponenter, vilket lovar att bana väg för ljusstarka och mer effektivare LECar för praktiska tillämpningar.

Publications

The thesis is based on the following publications:

I. Controlling the Emission Zone by Additives for Improved Light-Emitting Electrochemical Cells
Joan Ràfols-Ribé, **Xiaoying Zhang**, Christian Larsen, Petter Lundberg, E. Mattias Lindh, Cuc Thu Mai, Jonas Mindemark, Eduardo Gracia-Espino, and Ludvig Edman
Advanced Materials 2022, 34, 2107849

II. Efficiency Roll-Off in Light-Emitting Electrochemical Cells
Xiaoying Zhang, Joan Ràfols-Ribé, Jonas Mindemark, Shi Tang, Mattias Lindh, Eduardo Gracia-Espino, Christian Larsen, and Ludvig Edman
Advanced Materials 2024, 36, 2310156

III. Determining the Dynamic Emission Zone Width in Light-Emitting Electrochemical Cells
Xiaoying Zhang, Joan Ràfols-Ribé, Anton Kirch, Christian Larsen, and Ludvig Edman
In manuscript

IV. Impact of the Electrode Material on the Performance of Light-Emitting Electrochemical Cells
Anton Kirch, So-Ra Park, Joan Ràfols-Ribé, Johannes A. Kassel, **Xiaoying Zhang**, Shi Tang, Christian Larsen, and Ludvig Edman
ACS Applied Materials & Interfaces 2025, 17, 5184

Manuscripts not included in this thesis:

V. Pinpointing the Dynamic pin Junction
Joan Ràfols-Ribé, Atsushi Sato, Anton Kirch, **Xiaoying Zhang**, Sandra Jenatsch, Christian Larsen, Katsuhiro Marumoto, Ludvig Edman
In manuscript

Abbreviations

Ag	Silver
Al	Aluminium
Ca	Calcium
EDL	Electric Double Layer
EL	Electroluminescence
EQE	External Quantum Efficiency
EZ	Emission Zone
HOMO	Highest Occupied Molecular Orbital
ITO	Indium Tin Oxide
KCF_3SO_3	Potassium Trifluoromethanesulfonate
LEC	Light-emitting Electrochemical Cell
LED	Light Emitting Diode
LUMO	Lowest Unoccupied Molecular Orbital
OLED	Organic Light Emitting Diode
OSC	Organic Semiconductor
PLQY	Photoluminescence Quantum Yield
SY	Super Yellow
TMPE	Trimethylolpropane Ethoxylate
TMPE-OC	Octyl Carbonate end-capped Trimethylolpropane Ethoxylate
TMPE-OH	Hydroxyls end-capped Trimethylolpropane Ethoxylate

1 Introduction

Light-emitting electrochemical cells (LECs) are electroluminescent devices that convert electrical energy into light and their first introduction to the world is credited to Pei et al. in 1995.[1] The LEC structure is commonly simple, consisting of only a single active material, an emissive organic semiconductor (OSC) mixed with mobile ions, contacted by two electrodes. During operation, the redistribution of the mobile ions enables the *in situ* formation of electric double layers (EDLs) at the electrode/OSC interfaces and the subsequent electrochemical n- and p-doping of the OSC which finally results in the formation of a p-n junction doping structure.[2, 3]

This unique operational mechanism is the origin as to why LEC devices can feature bright area emission at a low operation voltage, as will be described in detail in this thesis. The formation of the EDLs enables for efficient charge injection even with high work-function and air-stable electrodes. Combined with that the active material is also air-stable (since potentially air-sensitive electrochemically doped OSC only forms when the device is powered), this allows for fabrication under ambient conditions.[4] Furthermore, since all components of the LEC can be soluble in solvents, the entire device can be cost- and energy-efficiently fabricated by fully solution-based printing techniques in ambient conditions.[5-10] A low-temperature printing fabrication also allows for the use of thin and flexible substrates. Photographs highlighting the possibilities of LECs are shown in Figure 1.1.

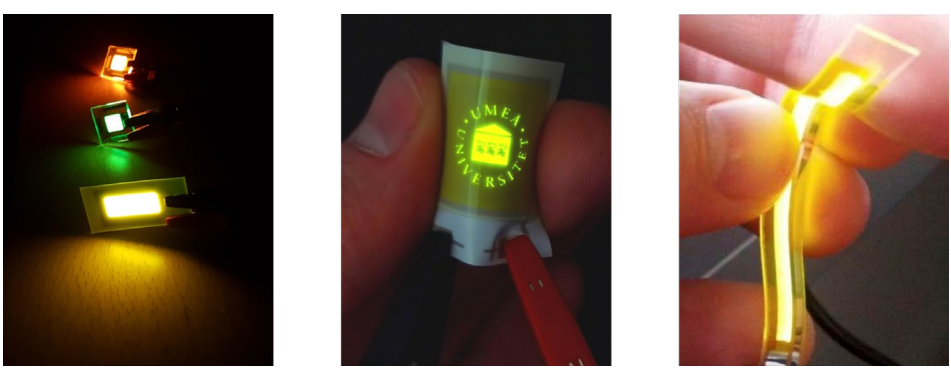

Figure 1.1. Photographs of thin and flexible LECs.

The features described above opens up for potential LEC applications where the current well-established light emitting diode (LED) and organic

light emitting diode (OLED) technologies fall short, primarily in terms of cost, sustainability and form factor. Apart from general lighting, possible LEC applications are typically portable (and therefore powered by an energy storage device or by integrated wireless energy harvesting) within for instance MedTech, packaging, signage, security and wearables, where the available input energy is limited. A critical requirement for these applications is thus a high emission efficiency, i.e. the efficiency at which the device converts electric energy into emitted light. However, to rationally design desired bright and efficient LECs, a detailed understanding of the complex LEC operational mechanism is needed.

Early investigations of the complex operational mechanism of LECs made use of a planar surface-cell configuration. In this configuration, two electrodes contacting the active material are deposited with a several mm interelectrode distance. During operation, the formed internal doping structure is exposed and it can therefore be visually observed and probed. Optical microscopy was used early on to image the electrochemical doping process.[11, 12] Together with Scanning Kelvin probe microscopy measurements of the electrochemical potential in the LEC during operation, these measurements on planar surface cell LECs enabled the verification of the so-called electrochemical doping model.[13, 14] Surface cells have further been used to, for instance, study the optimal doping concentration,[15] the device degradation processes,[16] the effects of different electrodes[17] and the electrolyte selection,[18] thus laying the early knowledge foundation of LEC operation.

For practical applications, the surface cell configuration is, however, severely limited due to their long turn-on times, low brightness and short lifetime. Instead, sandwich cells, in which a thin (~100-1000 nm) active material is sandwiched between the two electrodes, is the preferred structure since it can deliver fast turn-on times, long lifetimes and high brightness with the area emission pattern being defined by the electrode overlap.[19, 20] However, the thin active material in the sandwich configuration makes direct visual observations of the internal doping structure impossible. Instead, fundamental research on the LEC operational mechanism in sandwich cells has focused on, for instance, drift-diffusion modelling,[21-23] impedance measurements,[21, 22, 24] angle-resolved electroluminescence spectroscopy and optical modelling.[21, 25 26]

This thesis contributes to the knowledge of the complex operation of sandwich-cell LECs. The thesis starts by presenting the basic device structure, the materials, the device fabrication, and the electrochemical doping operational model in Chapter 2. This is followed by a description

of the injection and transport of electrons and holes, the electron and hole recombination into excitons, and the emission of photons in an LEC in Chapter 3. A method to characterize the structure of the emission zone (EZ) in sandwich-cell LECs, using the optical microcavity effect by comparing measured and simulated angle-resolved electroluminescence (EL) spectra, is presented in Chapter 4. Finally, in Chapter 5, this method is applied on LEC devices to extract the dynamic EZ position and width, to investigate and quantify the internal loss factors, and to establish a method for tuning the doping structure by active-material additives for improved emission efficiency.

2 Fundamentals of the light-emitting electrochemical cell

In this chapter, the device structure, the key material components, and the fabrication of the model LEC device studied in this thesis are described. We will present the complex LEC operation, which includes EDL formation, electron and hole injection, electrochemical p- and n-doping, and a p-n junction formation. We will also discuss and present the achievement of steady state and baseline performance metrics such as the forward luminance and the voltage.

2.1 Device structure

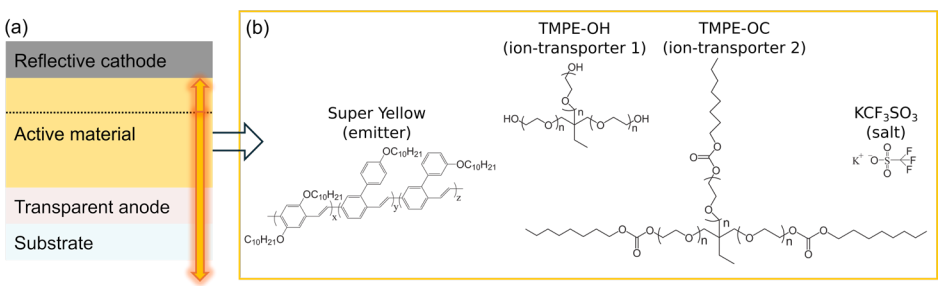

Figure 2.1. (a) The bottom-emitting sandwich-cell LEC and (b) the chemical structures of the active material constituents used in this thesis.

The LECs studied in this thesis are sandwich-cell devices, which are invariably fabricated on a robust glass substrate, as shown in Figure 2.1a. A thin layer of transparent indium tin oxide (ITO) was coated on the glass substrate, and it was herein biased as the positive electrode (anode). The active material consists of a blend of an emitter and an electrolyte. The chemical structures of the active material component used in this thesis are presented in Figure 2.1b. The presented "emitter" is both responsible for the transport of the holes and electrons, for the recombination of the holes and electrons to excitons, and the conversion of the excitons to photons. The utilized electrolyte comprises an ion-transporter that dissolves the salt ions in order to provide the mobile ions required for the LEC operation.[27]

In this work, we focused on one emitter: a phenyl-substituted poly(para-phenylene vinylene) conjugated copolymer, commonly termed "Super Yellow" (in short, SY). The electrolyte consists of a potassium trifluoromethanesulfonate (KCF_3SO_3) salt, containing a positively charged K^+ cation and a negatively charged $CF_3SO_3^-$ anion, that is dissolved by a branched trimethylolpropane ethoxylate (TMPE) ion-transporter, which is end-capped with either short and hydrophilic hydroxyl groups (TMPE-OH) or longer and more hydrophobic octyl carbonate groups (TMPE-OC). A thin layer of reflective aluminum (Al) serves as the top negative electrode (cathode).

The sandwich-cell LEC must contain at least one (semi)transparent electrode to allow the light generated in the active material to leave the device. The light generated in the active material can either directly leave the device through the transparent electrode or be reflected at the reflective electrode before leaving the device at the transparent electrode. This results in the device being either top-emitting or bottom-emitting depending on the arrangement of the electrodes.[28] The light is emitted at the opposite side of the substrate for a top-emitting device, and through the transparent bottom electrode and substrate for a bottom-emitting device. The latter configuration, as shown in Figure 2.1a, is used in this thesis. We further mention that the two utilized electrode materials (ITO and Al) are flat, hard and ion impermeable.[29] The LEC devices studied in this thesis are well-studied model systems that feature high luminance, low voltage and stable operation, which render them a good fit for reliable characterization.[21, 22, 26]

The primary sandwich-cell LEC investigated in this thesis is glass/ITO/SY:TMPE-OH:KCF_3SO_3/Al, with the mass ratio of the active material constituents being 1:0.1:0.03. This device, referred to as the TMPE-OH LEC, serves as the reference LEC system unless stated otherwise. An alternative sandwich-cell LEC equipped with the same substrate and electrode materials, but with ion-transporter being TMPE-OC (instead of TMPE-OH) and with the SY:TMPE-OC:KCF_3SO_3 mass ratio being 1:0.2:0.03 is referred to as the TMPE-OC LEC.

2.1.1 Emissive organic semiconductor

The conjugated polymer SY (chemical structure presented in Figure 2.1b) is an organic semiconductor. It comprises an organic conjugated system, containing alternating single and double carbon-carbon bonds. The overlapping p_z-orbitals allows delocalization of the π-electrons along the conjugated system.[30, 31] In OSCs, the distributions of the highest occupied

states and the lowest unoccupied states are separated in energy, and the difference between the highest occupied molecular orbital (HOMO) and the lowest unoccupied molecular orbital (LUMO) is called the energy gap.

An electron or a hole (i.e. the absence of an electron in the HOMO level) can be injected from an electrode into the LUMO or the HOMO of the OSC, respectively.[32] The injected electron or hole can be transported along overlapping p-orbitals along or between the conjugated system in the OSC. The electron or hole interacts strongly with the surrounding soft OSC, resulting in a local structural distortion and a polarization of the surrounding environment. The charge carrier and its surrounding polarization can be described as a quasiparticle called polaron.[33]

The mobile charge carriers in the OSC give rise to electrical conductivity, σ, which can be expressed as[34]

$$\sigma = qn_{\mathrm{e}}\mu_{\mathrm{e}} + qn_{\mathrm{h}}\mu_{\mathrm{h}} \tag{2.1}$$

where q is the elementary charge, n and μ are the charge density and mobility, respectively, with the subscripts e and h indicating electrons and holes, respectively. This equation shows that both the density and the mobility of the charge carriers determine the conductivity. The mobility refers to the velocity with which the mobile electrons (or holes) move through the available distributed states, i.e., the LUMO (or the HOMO), under an applied electric field.

The conductivity of an OSC can be drastically increased through a process known as “doping”, which involves increasing the number of mobile electronic charge carriers, i.e., the n factor in Eq. 2.1, through the addition of a dopant. In the case of LECs, the injected electrons and holes are electrostatically compensated by migration of mobile electrolyte ions in a process called electrochemical doping. This results in the formation of a charge-neutral doping complex, with the electron being compensated by a positive cation and the hole being compensated by a negative anion.[35] This added doping charge can greatly increase the charge carrier density in the LUMO (n-type doping) or HOMO (p-type doping), i.e., n_{e} or n_{h} in Eq. 2.1, with an upper limit determined by the number of ions included into the active material.[15, 18] It is worth mentioning that doping can also be in the form of chemical doping, where the electron is either transferred to the OSC from the chemical dopant species or vice versa.[36] However in this thesis, the focus is solely on the electrochemical doping that is a characteristic feature during the initial LEC operation.

An electron-hole pair can be created in an OSC by the optical excitation of an electron from the HOMO to the LUMO.[37, 38] Because of electrostatic attraction, the electron-hole pair can form a charge-neutral species called an exciton. The energy required to separate the electron and the hole in the exciton is called the exciton binding energy. In OSCs, this binding energy is on the order of ~0.5 eV, which is much more than the 25 meV of thermal energy that is available at room temperature.[36] This makes it difficult to separate excitons in OSCs for the attainment of mobile electrons and holes. The strong exciton binding energy in OSCs also promotes exciton generation by the recombination of the electrons and holes injected from the different electrodes, i.e., the excitation in response to an electric current called electrical excitation.[38] The exciton will decay after a certain lifetime by the electron falling back into the hole, and the released energy is either in the form of heat (non-radiative decay) or light emission (radiative decay).

2.2 Fabrication techniques

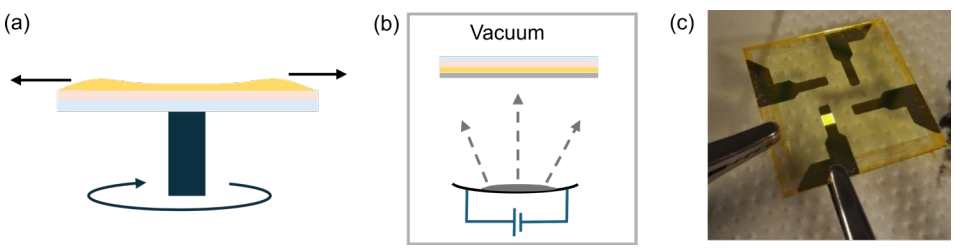

Figure 2.2. The fabrication method of (a) spin coating and (b) physical vapor deposition. (c) Photograph of a substrate with 4 fabricated LECs on top, and with one device being driven to uniform yellow emission.

2.2.1 Spin coating

The LEC devices in this thesis are made on prefabricated commercial ITO-coated glass substrates, which means that we only deposited the active material layer and the top cathode. The active material film is fabricated by spin coating, a solution-based technique (see Figure 2.2a), which uses the centrifugal force to spread out the active-material ink evenly over the spinning ITO-coated substrate. We first prepared three master inks by separately dissolving SY, TMPE (-OH or -OC) and KCF_3SO_3 at desired concentrations in cyclohexanone. These master inks were mixed in a desired mass ratio to prepare the active material ink. In the spin coating process, the substrate is positioned at the center of the rotating plate and fixed in place using vacuum suction. The active material ink is dropped and distributed to evenly cover the whole middle area of the substrate as

quickly as possible, followed by the spin coating procedure where the substrate is spun at a fixed ramp-up time, speed and time. After spin coating, the film is dried at a set temperature on a hotplate to remove residual solvent. The thickness of the dry active-material film was controlled by adjusting the spin coating parameters and the ink concentration. In this thesis, we used the spin-coating technique to produce uniform active-material films with low roughness, and with the thickness ranging from 100 ± 5 nm to 400 ± 10 nm, as measured by a profilometer. We note that the thickness variation increased for the thicker films. We also mention that the edges of the substrate may exhibit a pile-up of thicker active material, especially when a low spinning speed is used to produce thick films. However, since the measured emission area is selected to be small and located away from the edges (see Figure 2.2c), this inhomogeneity is found to not affect the device performance.

2.2.2 Physical vapor deposition

On top of the dry active material layer, the cathode is fabricated by physical vapor deposition under high vacuum (< 8×10^{-6} mbar), as illustrated in Figure 2.2b. A small number of metal pellets are placed in a tungsten boat crucible and heated via Joule heating by increasing the electrical current directed through the crucible. When the metal pellets melt and start evaporating, the metal vapor deposits on the surface of the active material layer and forms a thin solid metal film. The high vacuum level is required to allow the metal vapor to reach the surface of the active material layer without reacting or colliding with other particles in the vacuum chamber. The thickness of the deposited metal film is measured by a quartz crystal situated next to the substrates during fabrication. The crucible current is decreased once the electrode thickness reached the desired value. The cathode film is structured by placing a shadow mask before the active material film. The spatial overlap between the two electrodes and the active material defines the emission area of the LEC, which is typically a 2.0×2.0 mm^2 square in this thesis, unless otherwise mentioned.

Four LECs are fabricated on each substrate, as shown in the photograph in Figure 2.2c, where one device is electrically driven to uniform yellow emission. The above ink preparation and device fabrication are performed in a pair of connected N_2-filled gloveboxes, with a low concentration of oxygen and water ($[O_2] < 1$ ppm, $[H_2O] < 1$ ppm), to minimize degradation due to side reactions with oxygen and water. When the LEC devices had to be measured outside of the glovebox, they were protected from

exposure to oxygen and water by attaching a glass cover lid using either a pressure-sensitive adhesive or a UV-curable epoxy.

2.3 Operational mechanism

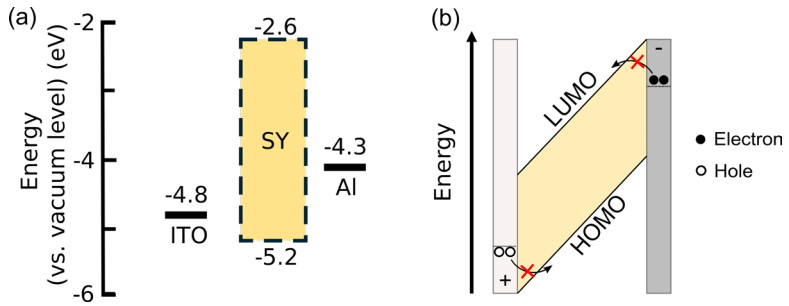

Figure 2.3. (a) Energy levels of the SY-based LEC at open-circuit condition. (b) Schematic diagram illustrating the energy levels and charge carriers' distribution in a device with large injection barriers but without mobile ions at a low forward bias condition.

Figure 2.3a presents the energy diagram at open circuit condition for the SY-based LEC (with an ITO anode and an Al cathode) used in this thesis.[29, 39] The energy difference between the Fermi level of the ITO anode and the SY HOMO defines the hole injection barrier of 0.4 eV while the energy difference between the Fermi level of the Al cathode and the SY LUMO sets a much larger electron injection barrier of 1.7 eV. Figure 2.3b illustrates the energy diagram at low forward bias for a device with the same large injection barriers and no mobile ions.[40] At a low forward bias (but above the built-in voltage), the electron and hole injection into the intrinsic OSC is severely limited; and to overcome the high injection barrier and realize electron and hole injection, a large electrical bias is required.

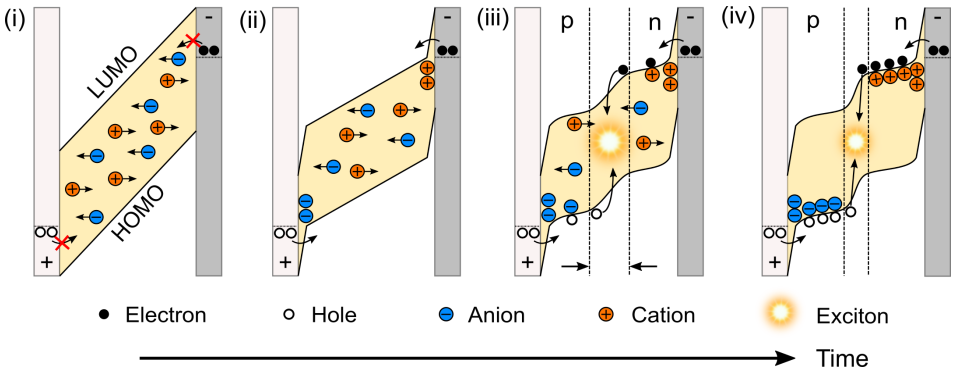

Figure 2.4. The transient operation of an LEC at applied bias: (i) the redistribution of the mobile ions, (ii) the formation of EDLs, enabling efficient and balanced charge carrier injection, (iii) the electrochemical doping of the OSC and the formation of the p-n junction, and (iv) the formation of the steady state EZ. Adapted from Ref. [41]

Luckily, the LEC contains mobile ions that help resolve this setback. When including these mobile ions in the active material, the transient operation of a functional LEC can be described by the following stages:[14, 42]

i. Initial ion redistribution (Figure 2.4, i): Once the device is biased, the mobile ions are redistributed in the active material under the influence of the applied electric field, i.e., the cations drift toward the negatively biased cathode and anions drift toward to the positively biased anode. At this stage, electrons and holes cannot yet cross the large energy barrier, so there is no charge carrier injection from the electrodes.

ii. EDL formation and charge carrier injection (Figure 2.4, ii): These redistributed uncompensated ions accumulate and form EDLs at the electrode/active material interface. The EDLs screen the electrostatic potential near the interfaces, resulting in a thinning of the injection energy barriers, which finally enables injection through tunnelling of electrons and holes into the LUMO and HOMO of the OSC, respectively.

iii. Electrochemical doping and p-n junction formation (Figure 2.4, iii): The injected electronic charge carriers reduce or oxidize the OSC, and are electrically compensated by counterions from the electrolyte to maintain charge neutrality. The doped OSC site and the corresponding compensating ion constitute an electrochemical doping unit. The initial doping happens close to the electrode as

charges are beginning to be injected, but the doping region grows further into the film as more charges are injected. The injected charge carriers are transported by hopping between adjacent sites in the high-conductivity doped regions. Finally, the doping fronts meet to form a p-n junction, where the electrons and holes can meet and recombine into excitons that can finally radiatively decay to a photon in the region defined as the EZ. The distribution of emissive excitons in the EZ is described by an exciton generation profile.

iv. Steady state (Figure 2.4, iv): As more charge carriers are injected, the doped regions grow toward each other, resulting in a narrowing EZ. The ions in the doped regions diffuse from the high concentration area until the ion diffusion and drift currents are balanced, resulting in no net motion of ions. This state is defined as the steady state.

2.3.1 Forward luminance and voltage

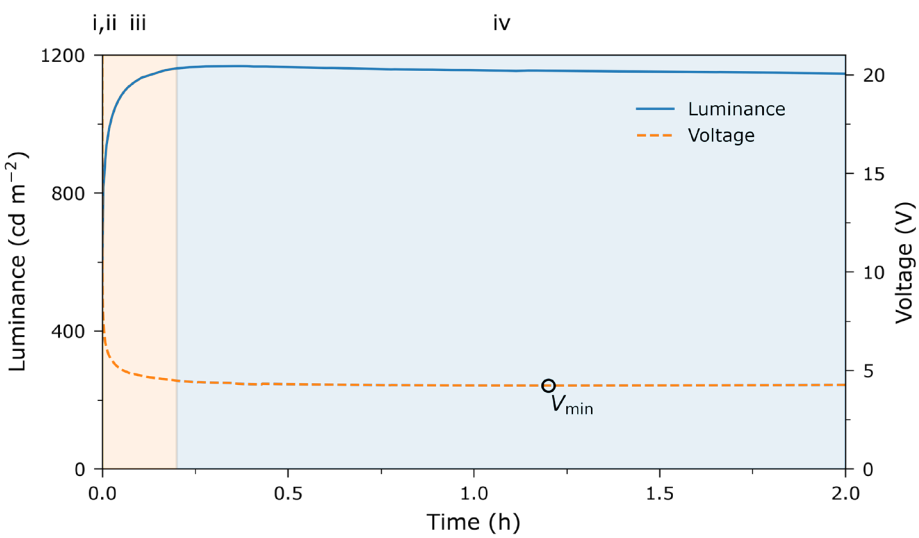

Figure 2.5. Transient forward luminance (solid blue line) and voltage (dashed orange line) at the different stages for a TMPE-OH device operated with a constant current density of 25 mA cm^{-2}. The four stages of LEC operation are indicated by the shaded areas with markers i-iv over the figure. Stages i and ii are observed just after turn-on, stage iii up until ~0.2 h (orange shaded area) and stage iv after ~0.2 h (blue shaded area).

An example of a typical TMPE-OH LEC performance is presented in Figure 2.5, where the forward luminance and the voltage of a device, operated with a constant current density of 25 mA cm^{-2}, are indicated by the solid blue line and dashed orange line, respectively.

The driving voltage drops rapidly during the initial operation (from stage i - iii), which is a characteristic feature of a functional LEC. This voltage drop indicates the formation of injection-facilitating EDL and the following transport-enhancing electrochemical doping of the OSC. Figure 2.5 shows that in stage i, the high resistance of the undoped OSC results in a high initial voltage. With the efficient charge carrier injection and subsequent formation of the electrochemical doping in stages ii and iii (orange shaded area in Figure 2.5), the conductivity of the active material is improved, resulting in the observed decrease in voltage.

Before electrons and holes can be injected into the active material (stage i), there is no light emission. In stages ii-iii, the forward luminance increases rapidly since the charge balance improves and the number of electrons and holes available to recombine into emissive excitons increases. The luminance increases to reach a peak value before the voltage decreases to the minimum. In this specific LEC, the luminance after the peak is observed to decrease slightly. This is mainly due to EZ changes during the final reorganization towards steady state, as will be explained further in Chapter 5.

As the electrochemical doping reaches equilibrium (stage iv), the drift and diffusion motion of the ions finds a balance, resulting in stable operation with very slow changes, as observed in Figure 2.5 at >0.2 h (blue shaded area). Eventually the minimum voltage, indicated by the circle black marker in Figure 2.5, is achieved. We define this point as the steady state.

3 Understanding the emission efficiency

The emission efficiency is commonly quantified by the external quantum efficiency (EQE), which is defined by the ratio between the number of emitted photons exiting the device per second and the number of electrons supplied by the driving circuit per second.[43] Considering the different transformations and loss pathways that electrons undergo to generate an emitted photon, the EQE can be factorized as follows:[44, 45]

$$\mathrm{EQE} = \eta_{\mathrm{exc,form}} \times \eta_{\mathrm{exc,rad}} \times \left(1 - \eta_{\mathrm{exc,loss}}\right) \times \eta'_{\mathrm{out}} \qquad (3.1)$$

where $\eta_{\mathrm{exc,form}}$ is the exciton formation efficiency, $\eta_{\mathrm{exc,rad}}$ is the fraction of excitons that are allowed to decay radiatively by spin statistics, $\eta_{\mathrm{exc,loss}}$ is the combined exciton losses, and η'_{out} is the effective outcoupling efficiency,[46] i.e., the product of the effective photoluminescence quantum yield (PLQY), $\mathrm{PLQY_{eff,}}$ and the outcoupling efficiency, η_{out}. Based on Eq. 3.1, an estimate of the maximum EQE for a fluorescent light-emitting device is 5 % using the following assumptions:[47]

i. A perfectly balanced injection, i.e., $\eta_{\mathrm{exc,form}}$ = 100 %.
ii. Only singlet excited states can decay radiatively, i.e., $\eta_{\mathrm{exc,rad}}$ = 25 %.[48]
iii. No exciton losses are present, i.e., $\eta_{\mathrm{exc,loss}}$ = 0 %.
iv. The effective outcoupling efficiency is 20 % and $\mathrm{PLQY_{eff}}$ = 100 %.[49-52]

In this chapter, the definitions of these efficiencies and how to estimate them are presented.

3.1 External quantum efficiency

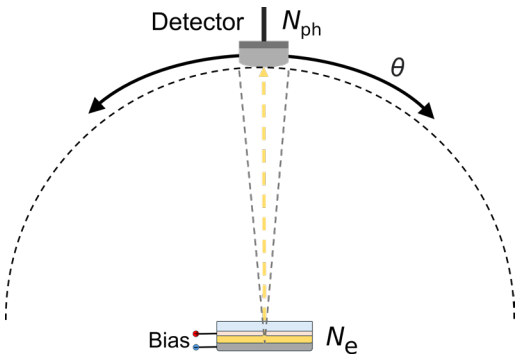

Figure 3.1. A schematic that illustrates how a photodetector is used to measure the EL spectral radiant intensity for a device under bias at different emission angles. Adapted from Ref.[41]

Although the EQE is commonly estimated based on certain assumptions as previously discussed, it can be determined more accurately through the experimental measurement of the EL spectral radiant intensity at different emission angles, θ, illustrated in Figure 3.1.[53] The EQE is defined as:

$$\mathrm{EQE} = \frac{N_{\mathrm{ph}}}{N_{\mathrm{e}}} \tag{3.2}$$

where N_{ph} is the number of photons per second escaping the device and N_{e} is number of electrons per second supplied by the driving circuit. N_{e} can be calculated as:

$$N_{\mathrm{e}} = \frac{I_{\mathrm{LEC}}}{q} \tag{3.3}$$

where I_{LEC} denotes the current through the LEC device and q is the elementary charge. N_{ph} is calculated by integrating the product of the spectral radiant intensity and its wavelength over all measured wavelengths (λ) and emission angles (θ) with the equation:

$$N_{\mathrm{ph}} = \frac{2\pi}{hc}\int_0^{\frac{\pi}{2}}\left(\int_{\lambda_{\mathrm{min}}}^{\lambda_{\mathrm{max}}} I(\lambda,\theta)\cdot\lambda d\lambda\right)\sin\theta\, d\theta \tag{3.4}$$

where $I(\lambda, \theta)$ is the spectral radiant intensity in the units of W nm^{-1} sr^{-1}, $\lambda_{\min}$ ($\lambda_{\max}$) is the minimum (maximum) wavelength of the EL spectra, h is the Planck constant, c is the speed of light in vacuum, and the 2π factor comes from the integration of the azimuthal angle.

By combining Eqs. 3.2-3.4, the full expression for the EQE in percentage is given by

$$\mathrm{EQE} = 100 \cdot \frac{2\pi q}{hcI_{\mathrm{LEC}}} \int_0^{\frac{\pi}{2}} \left(\int_{\lambda_{\min}}^{\lambda_{\max}} I(\lambda, \theta) \cdot \lambda d\lambda \right) \sin\theta \, d\theta \tag{3.5}$$

We thus explicitly calculate the EQE using Eq. 3.5 from the measured current through the LEC device, I_{LEC}, and the experimentally determined spectral radiant intensity, $I(\lambda, \theta)$.

3.2 Exciton formation efficiency

Electrons and holes are injected from the electrodes into the active material and transported on the OSC until they meet each other and recombine to form excitons. The efficiency of this process is described by the first factor in Eq. 3.1, i.e., the exciton formation efficiency, $\eta_{\mathrm{exc,form}}$. It is defined as the ratio between the number of generated excitons per second, N_{ex}, and the number of electrons per second supplied by the driving circuit, N_{e}, i.e.,

$$\eta_{\mathrm{exc,form}} = \frac{N_{\mathrm{ex}}}{N_{\mathrm{e}}} \tag{3.6}$$

The exciton formation efficiency depends on the electron and hole injection and recombination. For a functional LEC, the formation of EDLs and p- and n-doping structures results in an efficient and balanced charge carrier injection, and a recombination efficiency of the electrons and holes of one.

3.3 Radiative exciton fraction

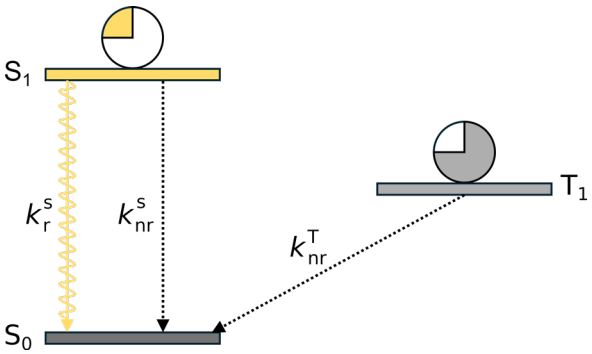

Figure 3.2. A simplified Jablonski diagram of the relevant transitions, showing the radiative and the non-radiative paths in a singlet emitter between the first excited singlet state (S_1), the first excited triplet state (T_1) and the ground state (S_0).

Excitons formed by electrical excitation can exist in either an excited singlet or triplet state, depending on their spin configuration.[32] Spin statistics predict that the ratio between the singlet and triplet states is 1:3.[54, 55] Since only singlet excitons can undergo radiative decay in a singlet emitter, the fraction of excitons that can emit light, $\eta_{\mathrm{exc,rad}}$ (second factor in Eq. 3.1) is 0.25.[45] Figure 3.2 shows a simplified Jablonski diagram only including the relevant transitions for a fluorescent emitter.[41] The radiative decay path is from the first excited singlet state (S_1) to the ground state (S_0) with a rate of $k_{\mathrm{r}}^{\mathrm{S}}$. This transition path can also be non-radiative with a rate of $k_{\mathrm{nr}}^{\mathrm{S}}$. The path from the first excited triplet state (T_1) to the ground state in a fluorescent emitter is spin-forbidden and, therefore, is only non-radiative with a rate of $k_{\mathrm{nr}}^{\mathrm{T}}$.

The decay rates for the singlet exciton define the intrinsic quantum efficiency, q_0, as[56]

$$q_0 = \frac{k_{\mathrm{r}}^{\mathrm{S}}}{k_{\mathrm{r}}^{\mathrm{S}} + k_{\mathrm{nr}}^{\mathrm{S}}} \tag{3.7}$$

which sets an upper limit for the quantum efficiency of a singlet-emitter LEC. This intrinsic quantum efficiency is estimated using the intrinsic PLQY, $\mathrm{PLQY_{int}}$. The PLQY is defined as the ratio between the number of emitted photons and the number of absorbed photons in a photoluminescence experiment, and it can be measured using an integrating sphere.[56] The $\mathrm{PLQY_{int}}$ is measured in a solid emitter film in the

absence of a cavity, with the assumption that all absorbed photons lead to the formation of singlet excitons.[32]

However, when the exciton, which can be considered as an electrical dipole, is placed in an optical cavity, its radiative decay rate is modified.[57] Therefore, to account for the cavity, an effective PLQY, $\mathrm{PLQY_{eff}}$, has to be considered, which can be expressed:[46, 58, 59]

$$\mathrm{PLQY_{eff}} = \frac{\mathrm{PLQY_{int}} \cdot \mathrm{F}}{\mathrm{PLQY_{int}} \cdot \mathrm{F} + (1 - \mathrm{PLQY_{int}})} \tag{3.8}$$

where F is the Purcell factor, which accounts for the modified dynamics of the exciton inside the cavity. The effective PLQY is not explicitly presented in Eq. 3.1, since it is included in the effective outcoupling efficiency factor.

3.4 Exciton losses

Since excitons exist for a limited amount of time before decaying, they can diffuse around during their lifetime and interact with other excitons or polarons (i.e. the holes and electrons on the OSC), leading to the loss of excitons' energy in other ways than radiative decay. These bimolecular interactions of excitons with either polarons or other excitons can result in either exciton-exciton or exciton-polaron quenching.[55, 60, 61] These quenching processes are quantified by the exciton loss factor, $\eta_{\mathrm{exc,loss}}$, i.e. the third factor in Eq. 3.1. In the thesis, we focus on the singlet exciton losses, specifically exciton-exciton quenching and exciton-polaron quenching.

3.4.1 Exciton-exciton quenching

The exciton-exciton quenching depends on the concentration of excitons, which is determined by the driving current density, the lifetime of the excitons, and the recombination rate of electrons and holes. With increasing current density and longer lifetimes, the concentration of excitons increases, resulting in a stronger exciton-exciton quenching. The exciton forms in the p-n junction region, so the exciton-exciton quenching happens there. When the p-n junction region gets narrower, a higher-concentration of excitons and, therefore, a stronger exciton-exciton quenching is expected.

The singlet exciton generation comes from charge recombination as discussed in Chapter 2.1.1. A singlet exciton can also be generated via collisions between two triplet excitons, i.e., triplet-triplet exciton

annihilation.[62, 63] In some fluorescent devices, this quenching process can result in a higher $\eta_{\mathrm{exc,rad}}$ and a higher EQE than the estimated limit.[64] In this thesis, we do not consider the extra singlet exciton generation from the triplet-triplet exciton annihilation.

3.4.2 Exciton-polaron quenching

Exciton-polaron quenching depends on the concentration of both excitons and polarons. Polarons compensated by ions are located in the electrochemically doped regions, and their concentration is determined by the doping level in the active material layer. LECs commonly exhibit a high electrochemical doping level, which results in a high concentration of polarons. These ion-compensated polarons can be strongly localized due to their Coulomb interaction with the counterions, while the non-ion compensated polarons in the exciton generation region can be more mobile due to a weaker interaction with surrounding environment.[65] For singlet-OSC LECs, the exciton-polaron quenching can be serious due to the high concentration of polarons in the region where the excitons are formed.[66]

The exciton-exciton and exciton-polaron quenching will be further investigated by drift-diffusion modeling, as presented in Chapter 4.5. The simulated exciton quenching mechanisms are used to explain the observations in Paper II.

3.5 Outcoupling efficiency

The excitons can decay radiatively by generation of photons, but these photons need to escape the device structure to be useful in applications (see Chapter 1). During their path through the LEC multilayer structure, and before being outcoupled, the generated photons can lose their energy to many different optical modes, which will be described in the next section. The outcoupling efficiency (η_{out}) is the quotient between the photons that make it out of the device and the photons generated inside the device.[67, 68] It is part of the effective outcoupling efficiency, η'_{out}, i.e. the last factor in Eq. 3.1, in the expression $\eta'_{\mathrm{out}} = \mathrm{PLQY_{eff}} \cdot \eta_{\mathrm{out}}$.

3.5.1 Optical modes in a microcavity

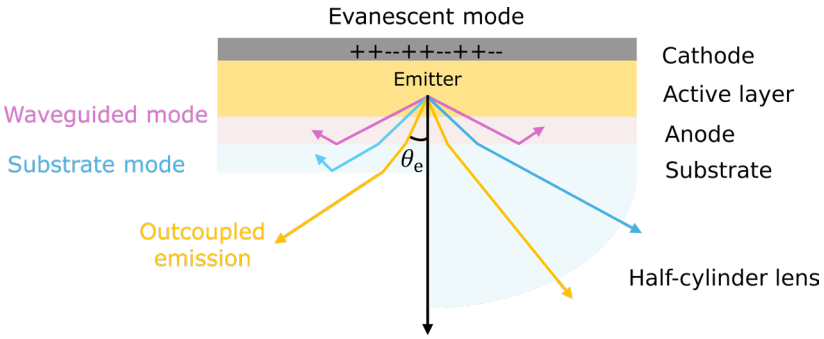

Figure 3.3. A schematic illustration of a thin-film emissive device and the different optical loss channels.

Only the outcoupled photons are useful for practical applications while the others are lost as the light propagates through the thin-film stack, i.e., the planar microcavity.[69] As shown in Figure 3.3, the light is divided into different optical modes, and this division is heavily affected by the emission angle and the properties of the thin-film stack (e.g., the refractive index, extinction coefficient, and thickness of each layer).

Let us now look at the different optical loss modes. The excitons close to the cathode can be lost to the evanescent mode, indicated by the black signs in Figure 3.3, which results from the near-field coupling of excitons to surface plasmon polaritons at the active-material/metallic interface. The light emission can further be divided into waveguided, substrate and outcoupled modes, depending on the emission angle, θ_e. Total internal reflection can happen when the light is incident on a layer with a lower refractive index. The light beam with an angle larger than the critical angle is coupled to and lost in waveguided and substrate modes. The substrate mode can be recovered by attaching a half-cylinder lens onto the substrate surface, as illustrated in Figure 3.3. The absorption mode (not shown in Figure 3.3) corresponds the photons that are absorbed in the device stack.[46]

3.5.2 Extraction of outcoupling efficiency

We are now interested in the measurement of the fraction of the outcoupled light. Since the photons generated in the active material layer cannot be measured experimentally, the outcoupling efficiency cannot be directly extracted. Instead, we use a commercial optical simulation software to determine the outcoupling efficiency of our thin-film emissive devices (see Chapter 4.2).

In summary, the excitons are either non-radiative or radiative, and the radiative excitons (i.e. the photons) are either outcoupled, or coupled into the absorption, waveguided, substrate or evanescent mode. The optical model used to calculate the relative fraction of each of these modes will be presented in Chapter 4.4. Specifically, we will focus on the determination of the effective outcoupling efficiency.

3.5.3 Interference effects in an LEC

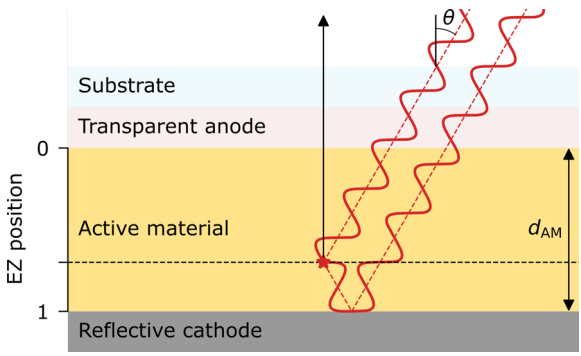

Figure 3.4. The interference effect in an LEC. The presented upper light wave with an emission angle of θ can optically interfere with the other depicted light wave, originating from the same spot, but which is first reflected off the cathode.

The outcoupling efficiency is affected by whether the emitted light waves feature constructive or destructive interference within the microcavity, formed between the strongly and weakly reflective interfaces in the thin-film device. This interference effect is sketched in Figure 3.4, which shows two emitted light waves (red lines) generated simultaneously from the same spot (red star marker) in the EZ. One light wave directly leaves the device with an emission angle θ, while the other leaves the device with the same emission angle but after first being reflected at the cathode. These two light waves interfere constructively if the phase difference between them is an even multiple of π, i.e., they are in phase. A phase difference of an odd multiple of π results in destructive interference. This explains why the properties affecting the phase difference, such as the thickness and the refractive index of the active material,[70] the phase shift at the interface,[71] and the distance of the EZ to the reflective interface[72, 73] are critical for the EL spectra and outcoupling efficiency.

4 Determination of the emission zone and the efficiency

In this chapter, we describe how to determine the EZ position and width by exploiting the microcavity effect. For that end, we measure the angle-resolved EL spectra and intensity with a spectrogoniometer setup and simulate the same data with an optical model based on a transfer matrix formalism. Once we have determined the EZ position and width, we can use the same optical model to simulate the optical modes, described in Chapter 3.5.1, including the outcoupled light and the loss channels. Furthermore, we describe the numerical drift-diffusion model used to simulate the doping structure and to understand and explain the formation of the EZ and its positional shift. Additionally, this model is employed to simulate the exciton decay and quenching rates, which cannot be simulated by the optical model.

4.1 Spectrogoniometer setup

4.1.1 Conventional setup

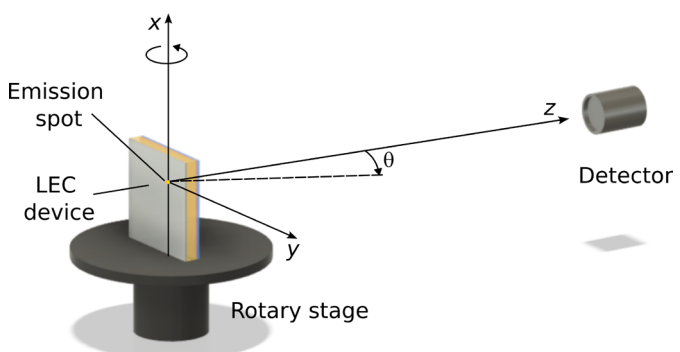

Figure 4.1. A sketch of the conventional spectrogoniometer setup used to measure the angle-resolved EL spectrum. It shows that the device on the left side can be rotated at an angle of θ while the detector measures the EL spectra and intensity.

By taking advantage of the microcavity effect described in Chapter 3.5.3, the EZ position and width can be determined using the measured and simulated angle-resolved EL spectra and intensity. While the EZ position in principle can be estimated using the EL spectrum at a single angle,

analyzing the EL spectra and intensity for multiple angles allows for a more accurate determination of the EZ position.[74]

The angle-resolved EL spectra are measured by a custom-built spectrogoniometer setup, as sketched in Figure 4.1. The measurement goes as follows. First, the LEC device under study is aligned with the rotation axis of a stepper motor. The rotation angle defines the viewing angle, θ, varying from -90° to 90°, with 0° corresponding to the forward direction. The emitted light is collected by a collimating lens and detected by a spectrometer. Then, the EL spectra and intensity at different angles are recorded by rotating the device. We will refer to this relatively simple setup as the conventional setup.

4.1.2 Refined setup

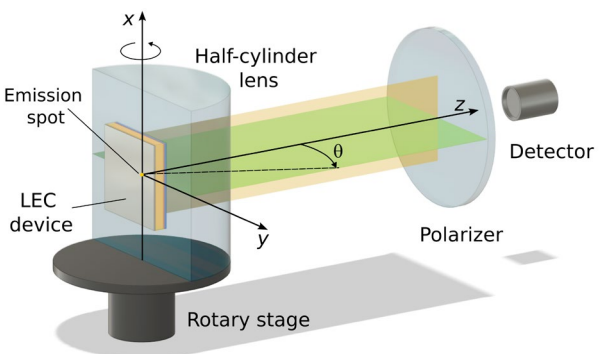

Figure 4.2. A sketch of the refined spectrogoniometer setup.[26] A half-cylinder lens is attached to the substrate of the LEC device, and a linear polarizer is inserted before the detector.

The conventional spectrogoniometer setup has limitations. Since unpolarized light is measured, the EZ extraction requires knowledge of the value of the anisotropy coefficient,[26] i.e., the fraction of vertical emissive dipoles to the total number of emissive dipoles, which will be described in Chapter 4.2. Another limitation is that a lot of light is trapped in the substrate, which causes a low intensity of the measured EL spectra at high angles. In order to overcome these limitations, we did two refinements to the measurement setup.

First, a linear polarizer is included, as schematically depicted in Figure 4.2. This eliminates the requirement of knowledge of the (often unknown) anisotropic coefficient of the emissive OSC. The linear polarizer before the detector only allows a specific linear polarization of the light to pass

through. The s-polarized light beam (electric field oscillating in the yellow plane in Figure 4.2) only includes a contribution from the horizontal dipoles, while the p-polarized light beam includes a contribution from both horizontal and vertical dipoles.[26] Therefore, the linear polarizer is aligned so that only the s-polarized light is measured, removing the uncertainty of the orientation distribution of the emissive dipole in the EZ extraction method. Specifically, the linear polarizer eliminates the necessity to know the orientation parameter in the optical model, which will be described in Chapter 4.2.

The other refinement of the setup is the employment of a half-cylinder lens, which enhances the measured EL intensity at large angles by extracting the light trapped in the substrate mode. Attaching the half-cylinder lens to the device significantly suppresses this loss to the substrate mode by eliminating total internal reflection at the glass/air interface, resulting in a higher signal in the measured EL spectra at high emission angles. The half-cylinder lens is attached to the glass substrate by an index-matched oil to optically eliminate the interface between the substrate and the half-cylinder lens.

4.2 Optical model

The light propagation through the LEC device, i.e., the planar multilayer structure, is modeled with a transfer matrix formalism implemented in the commercial software Setfos (Fluxim AB, Switzerland). A typical workflow for this optical modeling is as follows:[75]

- First, define the LEC multi-layer structure.
- Second, define the optical properties of each layer (refractive index, n, extinction coefficient, k, and thickness, d). The first two parameters can be wavelength dependent.
- Third, position an emitter, which is modelled as an emissive radiating dipole, in the emissive layer. The spatial distribution of excitons is described by the exciton generation profile, $f(x)$. The EL spectra of the emitter in free space are referred to as the intrinsic EL spectra, $I(\lambda)$. The anisotropy coefficient of the emissive dipoles, a, can be used to simulate the excitons' orientation.
- Last, propagate the intrinsic spectra of the emitter through the optical stack using the transfer matrix formalism. This formalism can calculate the EL spectra in the far field and the power distribution of the different optical modes (outcoupled,

absorption, waveguided, substrate, evanescent and non-radiative mode).

Now, we can simulate the angle-resolved EL spectra with this optical model, and then match it with the measured EL spectra to determine the unknown exciton generation profile, including the EZ position and width. Furthermore, using this extracted exciton profile, the optical model can also calculate the fractional power contributions of the different modes relative to the total dissipated power by the emissive dipoles, including the outcoupled and loss channels described in Chapter 3.5.1.

4.2.1 Simplified optical model

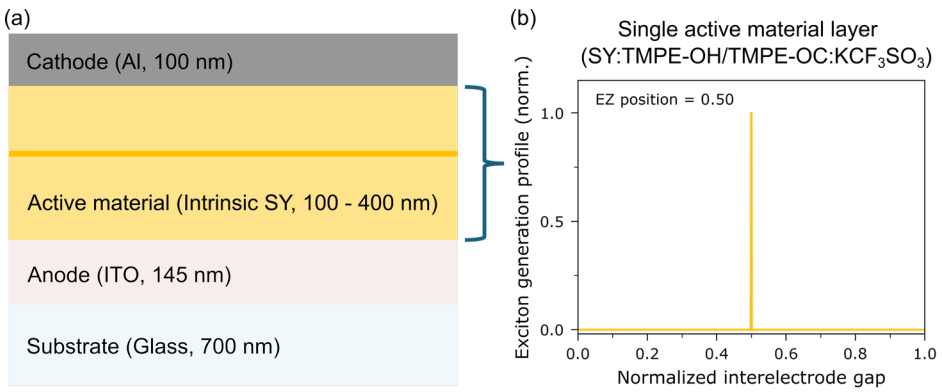

Figure 4.3. (a) The simulated LEC structure. (b) The exciton generation profile in the form of a delta function with the EZ positioned at 0.50.

The structure of the simulated LEC, with the same sandwich structure as the real device, is presented schematically in Figure 4.3a. It includes an active material layer between an Al cathode and an ITO anode, with the latter on top of a transparent glass layer. In this simplified optical model, the whole active material layer is defined as an emissive layer where excitons can be generated. The emissive layer is set to be transparent, which is a requirement in the optical model formalism.[46] The refractive index of the active material is that of an intrinsic SY film, as gleaned from Ref.[76].

The spatial distribution of the photons generated in the emissive layer is determined by the exciton generation profile. Since the emissive region of an LEC can be thin, the first approximation was that the exciton generation profile was a delta function. A number of different Gaussian-shaped exciton generation profiles were investigated in Ref.[25], but the

simulated EL spectra were found to be highly invariant to the EZ width. This shows that the sensitivity to the EZ width is small in comparison to that of the EZ position. Therefore, to extract the EZ position, the delta function is used for simplicity reason.

Figure 4.3b shows an example with the EZ positioned in the center of the active material layer. The EZ position is normalized to the active material thickness, and it thus ranges from 0 (when positioned at the anodic interface) to 1 (when positioned at the cathode interface). When this optical model was used in conjunction with the conventional spectrogoniometer setup, a value of the anisotropy coefficient, a, describing the orientation of the emissive dipoles, is required. In Paper I, this anisotropy coefficient is assumed to be 1/3, which corresponds to an isotropic dipole distribution.

To calculate the EL spectra emitted from an optical stack, information of the emission spectrum of the emitter in free space, referred to as the intrinsic emission spectrum, is required. The photoluminescence spectrum of a 17-nm SY film is used as the intrinsic spectrum in the optical model because the photoluminescence spectrum of thicker SY film (≥ 30 nm) exhibited pronounced cavity effects, as shown in Figure S7 in Paper I.

Now, the EL spectra of the light escaping from the device can be simulated as a function of EZ position using the presented model, and these data are used for the determination of the EZ position.

4.2.2 Advanced optical model

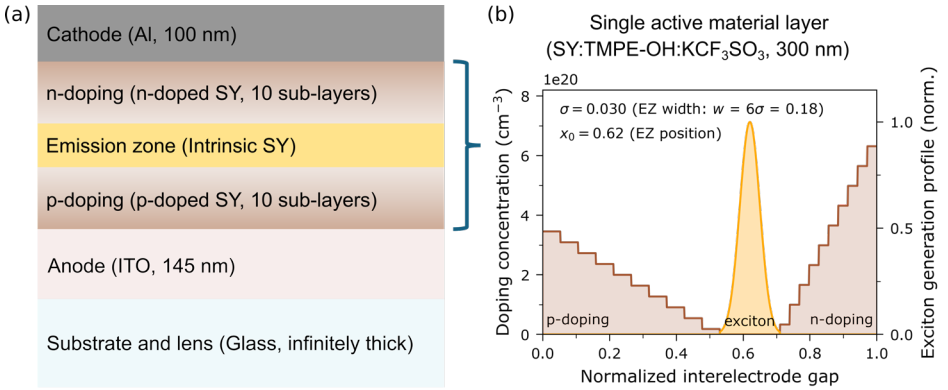

Figure 4.4. (a) The simulated LEC structure after refinement, comprising the p- and n-typed doping regions. (b) The simulated Gaussian-shaped exciton generation profile and the 10-sublayer p- and n-type doping regions.

The simplified optical model of the LEC structure, previously presented, does not account for the doping-dependent refractive index of the SY emitter, which may explain why the simplified optical model is insensitive to the EZ width. Figure 4.4a shows the modelled LEC structure after refinement that includes the p- and n-type doped regions, and which considers that the optical properties change with the doping level. This refined model also considers the effects of the half-cylinder lens, reflecting the refinement made to the spectrogoniometer setup shown in Chapter 4.1.2. In the model, an infinitely thick transparent glass layer mimics the combined effect of the glass substrate and the half-cylinder lens.

The two doped regions were modelled with constant doping concentration gradients, as shown in Figure 4.4b, with the highest doping concentration at the corresponding injecting electrode and a zero-doping concentration at the interface with the EZ. The exciton distribution in the EZ, as indicated by the yellow line in Figure 4.4b, is modelled as a Gaussian function:

$$f(x) = \frac{1}{\sigma\sqrt{2\pi}} e^{-\frac{1}{2}\left(\frac{x-x_0}{\sigma}\right)^2} \tag{4.1}$$

where x denotes the spatial position of excitons within the active material layer (normalized to its thickness), x_0 represents the peak of the exciton distribution, i.e. our proxy for the EZ position, and σ is a measure of the width of the exciton distribution.

To consider absorption in the doped regions, no emission is allowed to occur in these regions due to a requirement of the optical model. However, a Gaussian-shaped exciton profile will a priori incorporate the doped regions surrounding the EZ, and the exciton concentration is, therefore, set to 0 in the doped regions. This limitation results in that a small portion (less than 0.5 %) of the excitons are excluded from the simulation. The EZ width, w, is defined to be $w = 6\sigma$.

Now, the EL spectra can be simulated as a function of the EZ position and the EZ width, i.e., x_0 and w, using the advanced optical model. By matching the simulated EL spectra to the measured EL spectra, the EZ position and width can be extracted.

4.3 Fitting the EZ

With both the measured and simulated EL spectra available, the relevant parameters for the exciton generation profile can be extracted. We use the conventional spectrogoniometer setup and the simplified optical model for the extraction of the EZ position in Papers I and II. Later on, we utilize the refined spectrogoniometer setup and the advanced optical model to extract both the EZ position and width in Paper III.

4.3.1 Fitting the EZ position

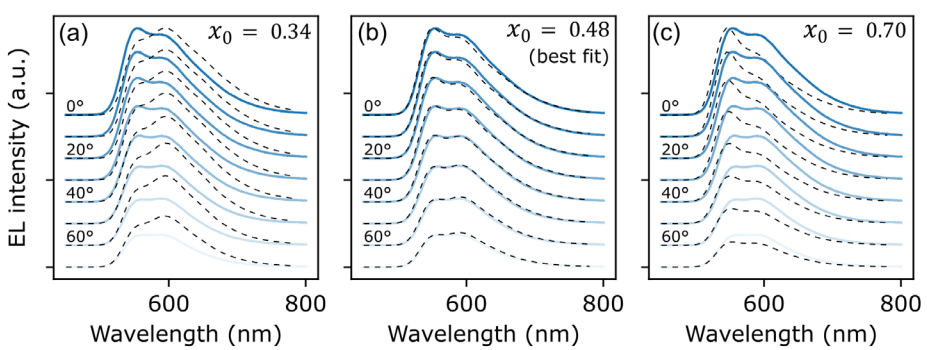

Figure 4.5. The measured (solid lines) and the simulated (dashed lines) angle-resolved EL spectra for different EZ positions, x_0, where x_0 is (a) 0.34, (b) 0.48 (corresponding to the best fit) and (c) 0.70.[77]

The EZ position is obtained by minimizing the root mean square error ($\mathrm{RMSE}(x_0)$, error for short) between the measured and the simulated angle-resolved EL spectra. The error is calculated as:[77]

$$\mathrm{RMSE}(x_0) = \sqrt{\frac{1}{N_\theta}\sum_\theta \frac{1}{N_\lambda}\sum_\lambda \left(I_{\theta,\lambda}^{\mathrm{meas}} - I_{\theta,\lambda}^{\mathrm{sim}}(x_0)\right)^2} \qquad (4.2)$$

where $I_{\theta,\lambda}^{\mathrm{meas}}$ and $I_{\theta,\lambda}^{\mathrm{sim}}(x_0)$ are the measured and simulated EL spectral radiant intensity, respectively. $I_{\theta,\lambda}^{\mathrm{meas}}$ is normalized to the maximum EL intensity at 0°, N_θ and N_λ are the number of the emission angles and wavelengths, respectively. Instead of performing a classical minimization algorithm presented in Ref.[74], a pre-calculated solution-landscape approach is used to speed up the computational time. A set of solutions, i.e., a solution landscape, for $I_{\theta,\lambda}^{\mathrm{sim}}(x_0)$ is generated with x_0 varying between 0.05 and 0.95 in steps of 0.01. The error landscape, i.e., the full set of errors, is calculated by inserting the solution error landscape into Eq. 4.2. By comparing all calculated errors, we ensure that the global minimum error is identified within a given resolution, determined by the discretization of x_0 in the solution landscape. The EZ position, corresponding to the global minimum error, represents the best-fitted EZ position.

One example of the measured and simulated EL spectra is presented in Figure 4.5b, which shows that the simulated EL spectra (dashed line) replicates well the measured spectra (solid line) for all angles for the best-fit EZ position case. For comparison, the simulated EL spectra for the other EZ positions of 0.34 and 0.70, as presented in Figure 4.5a and c, show a much stronger deviation from the measured EL spectra. This procedure is used in Papers I and II.

4.3.2 Fitting the EZ position and width

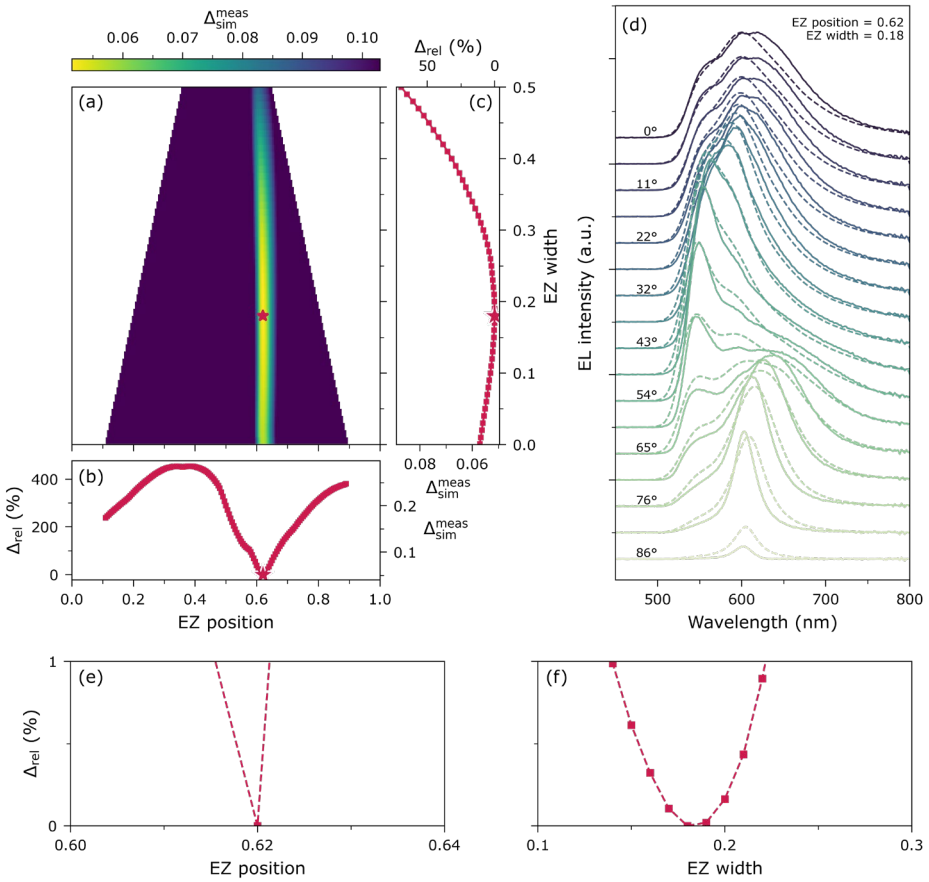

Figure 4.6. The extraction of the best-fit EZ position and width for a device at steady state when driven with a current density of 25 mA cm⁻². (a) The calculated 2D error landscape for the EZ position and width. (b) Right axis: the local minimum error for each simulated EZ position. Left axis: the local minimum relative error for each simulated EZ position, and a zoom-in plot with a maximal 1 % relative error is shown in (e). (c) Bottom axis: the local minimum error for each simulated EZ width. Top axis: the local minimum relative error for each simulated EZ width, and a zoom-in plot with a maximal 1 % relative error is shown in (f). The star marker in Figures (a-c) indicates the global minimum error position, corresponding to the best-fit EZ position and width. (d) The measured (solid lines) and best-fit (dashed lines) EL spectra as a function of the emission angle θ.

Both the best-fit EZ position and width are obtained by minimizing the error between the measured and simulated angle-resolved EL spectra and intensity by the refined spectrogoniometer setup and the advanced optical

model, as shown in Figure 4.2 and Figure 4.4. Since the mean absolute error treats all errors equally without assigning additional weight to larger errors,[78] and both linear and nonlinear fitting procedures perform reasonably well shown in Ref.[74], the mean absolute error ($\Delta_{\mathrm{sim}}^{\mathrm{meas}}(x_0, \sigma)$, error for short) is used here and is calculated as:

$$\Delta_{\mathrm{sim}}^{\mathrm{meas}}(x_0, \sigma) = \frac{1}{N_\theta} \sum\nolimits_\theta \frac{1}{N_\lambda} \sum\nolimits_\lambda \left| I_{\theta,\lambda}^{\mathrm{meas}} - I_{\theta,\lambda}^{\mathrm{sim}}(x_0, \sigma) \right| \tag{4.3}$$

where $I_{\theta,\lambda}^{\mathrm{sim}}(x_0, \sigma)$ is the simulated s-polarized EL spectral intensity as a function of EZ position and width. A 2D solution landscape with dimensions of 199 x 50 for $I_{\theta,\lambda}^{\mathrm{sim}}(x_0, \sigma)$ was generated with x_0 varying between 0.005 and 0.995 in steps of 0.005, and w varying between 0.01 and 0.50 in steps of 0.01. The error landscape was then calculated by inserting these solutions into Eq. 4.3. One example of the generated 2D error landscape is shown in Figure 4.6a, for a device at steady state when driven with a current density of 25 mA cm^{-2}. By comparing all the calculated errors, the global minimum error (red star marker in Figure 4.6a), $\Delta_{\mathrm{min}}(x_0, \sigma)$, is determined, and the corresponding EZ position and width are extracted.

Let's see an example of how this procedure is performed. Figure 4.6b, right axis, plots the local minimum error for each simulated EZ position, i.e., the minimum error among all simulated EZ widths at one specific EZ position. Figure 4.6c, bottom axis, plots the local minimum error for each simulated EZ width, i.e., the minimum error among all simulated EZ positions at one specific EZ width. Figure 4.6a, with support of b and c, confirms that the extracted EZ position and width, indicated by the star marker, correspond to the global minimum rather than a local minimum. Figure 4.6d presents the simulated EL spectra (dashed lines) that best fit the measured EL spectra (solid lines), with $x_0 = 0.62$ and $w = 0.18$. The observed agreement between the measured and best-fit EL spectra supports the validity of the fitting procedure.

To estimate the sensitivity of the presented method to the EZ position and width, the relative error, $\Delta_{\mathrm{rel}}(x_0, \sigma)$, is defined as:

$$\Delta_{\mathrm{rel}}(x_0, \sigma) = \frac{\Delta_{\mathrm{sim}}^{\mathrm{meas}}(x_0, \sigma) - \Delta_{\mathrm{min}}(x_0, \sigma)}{\Delta_{\mathrm{min}}(x_0, \sigma)} \times 100 \tag{4.4}$$

i.e., the relative error is the normalized error to the global minimum error. In this way, we can compare the sensitivity of the method to the EZ

position and the EZ width. Figure 4.6b, left axis, and 4.6c, top axis, present the relative error for each simulated EZ position and width, which shows that the maximum relative error for the simulated EZ position is significantly higher than that for the simulated EZ width. This observation shows that the simulated EL spectra deviate more from the measured EL spectra when the simulated EZ position is incorrect compared to when the simulated EZ width is incorrect.

The refined method is less sensitive to extracting the EZ width than the EZ position. A quantitative demonstration, with a maximum relative error of 1 % as an example, is indicated in Figure 4.6e-f. For a 1 % relative error margin, the EZ width ranges from 0.14 to 0.22 (a variation of 8 % of the whole active material layer), which is much wider than the range of the EZ position, which is essentially constant at 0.62 (the variation is smaller than the resolution of the solution landscape).

4.4 Determining the outcoupling efficiency

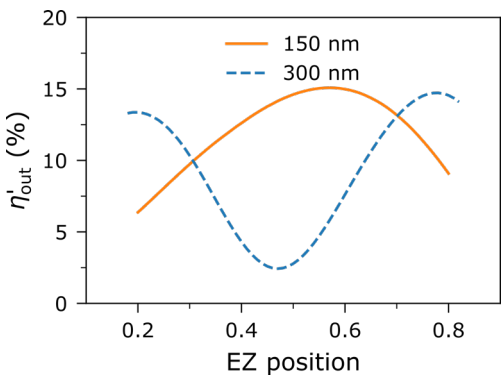

Figure 4.7. The simulated effective outcoupling efficiency as a function of EZ position for an LEC device with a 150 nm (orange solid line) and a 300 nm (blue dashed line) thick active material layer.

By using the extracted information about the EZ position and width, the effective outcoupling efficiency, as defined in Chapter 3.5, can be simulated using the same advanced optical model as described in Section 4.2.2.

In Paper II, we did however estimate the EZ width using the approach by Lindh et al.[25] The estimated EZ width and the extracted EZ position are the input to the advanced optical model to simulate the effective outcoupling efficiency. One example of the simulated effective outcoupling efficiency as a function of the EZ position is presented in

Figure 4.7 for an LEC device with a 150 nm (orange solid line) and a 300 nm (blue dashed line) thick active material layer. The effective outcoupling efficiency exhibits a strong undulation dependency on the EZ position, which is a direct reflection of the interference effect by the microcavity, as described in Chapter 3.5.3.

In paper III, after refining the spectrogoniometer setup and improving the optical model, both the EZ position and width could be extracted. The effective outcoupling efficiency in paper III is simulated based on these extracted EZ positions and widths.

The above simulations of the effective outcoupling efficiency are done with the software Setfos, and they consider the measured intrinsic PLQY of SY (= 60 %) and its modification due to the cavity in the calculation. Therefore, the maximum effective outcoupling efficiency is less than the estimated upper limit of ~20% for a device comprising a glass substrate and an isotropic emitter.[51, 52]

4.4.1 Loss modes

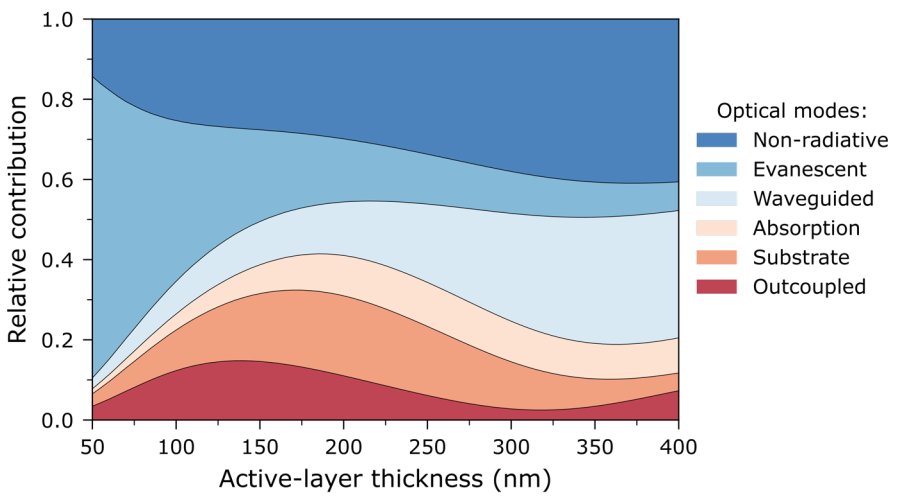

Figure 4.8. The simulated relative contributions of the outcoupled and the loss modes.

While the useful mode in terms of applications is the outcoupled mode, it is also interesting to understand how the remaining exciton energy is distributed, that is, to evaluate the contributions of the different loss channels.[25, 42] As mentioned in Chapter 3.5.2, the Setfos software simulates the relative contribution of each mode. Figure 4.8 presents the

relative contributions from the different loss modes as a function of the active-layer thickness, as calculated with the advanced optical model and a centered Gaussian exciton distribution with an EZ width scaling with the active-layer thickness, as presented in Ref.[25].

Figure 4.8 shows that the outcoupled mode has an oscillating dependency on the thickness of the active material layer. However, its contribution remains significantly smaller than that of the sum of the loss modes. For an LEC with a thick active layer above ~200 nm, the energy is mostly lost to the substrate and waveguided modes. The coupling to the evanescent mode is decreasing with increasing distance between the emitter and the cathode.[79] The loss to absorption increases with increasing thickness of the active material layer.[25] The simulated relative contribution of each optical mode, as a function of both the active-layer thickness and the EZ position, is presented in Figure S5 in Paper II. Such simulations can facilitate the rational design of efficient devices.

4.5 Electrical drift-diffusion model

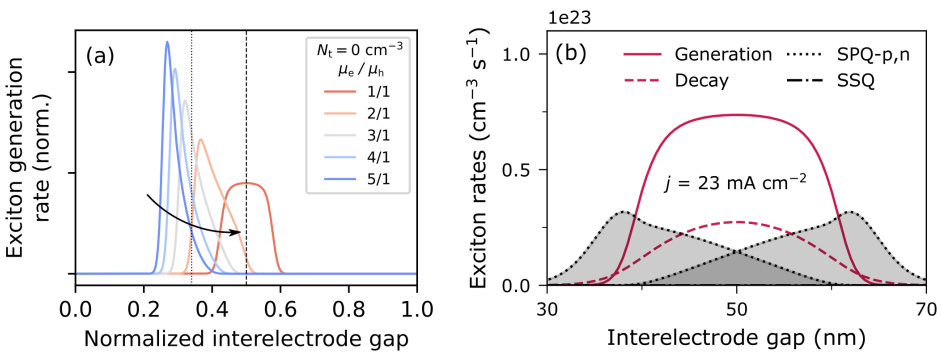

Figure 4.9. (a) The exciton generation profile for a trap-free active material at different electron and hole mobility ratios.[77] (b) The exciton generation, decay, and quenching rates as a function of the position in the interelectrode gap.[80]

The above optical model does not capture the exciton-exciton and exciton-polaron quenching, described in Chapter 3.4, which is a critical aspect affecting the LEC efficiency. Additionally, since the exciton generation profile is a key assumption in the optical model, knowing the exciton distribution is crucial for developing a more realistic and accurate optical model. To address these problems, we employ an electrical drift-diffusion model that describes charge carrier injection, transport and recombination, and exciton distribution in an LEC device, through numerically solving the drift-diffusion equations for all the charged

species, and the rate equation for the generated excitons. Further details of this electrical model can be found in Ref.[46, 75, 81].

Once the charge distribution is solved, the exciton rate equation can be solved. Excitons, formed by the recombination of electrons and holes, can diffuse to other locations before decaying either radiatively or non-radiatively. The rate equation for the time (t) and position (x) dependent singlet exciton density, $S(t,x)$, can be expressed as:[75]

$$\frac{dS(t,x)}{dt} = g \cdot R(t,x) + \vec{\nabla} \cdot \vec{J}(t,x) - k_{\mathrm{rad}} \cdot S(t,x) - k_{\mathrm{nonrad}} \cdot S(t,x)$$

$$-k_{\mathrm{SSQ}} \cdot S(t,x)^2 - k_{\mathrm{SPQ,p}} \cdot S(t,x) \cdot p(t,x) - k_{\mathrm{SPQ,n}} \cdot S(t,x) \cdot n(t,x) \quad (4.5)$$

where $p(t,x)$ and $n(t,x)$ denote the density of holes and electrons, respectively. The term $g \cdot R(t,x)$ is the singlet exciton generation term, where g is the exciton formation ratio, 0.25, and $R(t,x)$ is the Langevin recombination rate ($R(t,x) \propto p(t,x) \cdot n(t,x)$), which is defined as the ratio of electron-hole recombination events per second per unit volume.[38, 82] The term $\vec{\nabla} \cdot \vec{J}(t,x)$ is the exciton diffusion, where $\vec{J}(t,x) = D_S \cdot \vec{\nabla} S(t,x)$ is the exciton diffusion current. The constants k_{rad}, k_{nonrad}, k_{SSQ}, $k_{\mathrm{SPQ,p}}$ and $k_{\mathrm{SPQ,n}}$ in unit of s^{-1} are the radiative decay rate, the non-radiative decay rate, the exciton-exciton quenching rate, the exciton hole-polaron quenching rate and the exciton electron-polaron quenching rate, respectively. Since we are interested in the volumetric rates with unit of $cm^{-3}\ s^{-1}$, representing the number of excitons that decay or are quenched, the terms including the constant rate and the densities of excitons and charge carriers in Eq. 4.5 are used in this thesis. Therefore, $k_{\mathrm{rad}} \cdot S(t,x)$ is the radiative decay, $k_{\mathrm{nonrad}} \cdot S(t,x)$ describes the non-radiative decay, $k_{\mathrm{SSQ}} \cdot S(t,x)^2$ is the exciton-exciton quenching term, and $k_{\mathrm{SPQ,p}} \cdot S(t,x) \cdot p(t,x)$ and $k_{\mathrm{SPQ,n}} \cdot S(t,x) \cdot n(t,x)$ are the exciton hole-polaron and electron-polaron quenching terms with respective rates, $k_{\mathrm{SPQ,p}}$ and $k_{\mathrm{SPQ,n}}$. In Paper I, the transient EZ position is simulated for different ionic and electronic mobility ratios. In these simulations, the position of the peak exciton generation rate, $g \cdot R(t,x)$, is used to represent the EZ position.[83]

At steady state, the rate equation for the singlet exciton density fulfills the condition of $\frac{dS(t,x)}{dt} = 0$. Thus, Eq. 4.5 can now be expressed as:

$$g \cdot R(x) + \vec{\nabla} \cdot \vec{J}(x) = k_{\mathrm{rad}} \cdot S(x) + k_{\mathrm{nonrad}} \cdot S(x) + k_{\mathrm{SSQ}} \cdot S(x)^2 + k_{\mathrm{SPQ,p}} \cdot S(x) \cdot p(x) + k_{\mathrm{SPQ,n}} \cdot S(x) \cdot n(x) \quad (4.6)$$

Figure 4.9a shows an example of the exciton generation profile, $g \cdot R(x)$, at steady state for a trap-free active material with different electron-hole mobility ratios. The EZ position at steady state is dictated by the ratio of electron and hole mobility, μ_{e} and μ_{h}, and it can shift in the active material by a change in the electron:hole mobility ratio, as depicted in Figure 4.9a.

The exciton radiative decay rate, $k_{\mathrm{rad}} \cdot S(x)$, is indicated by the red dashed line in Figure 4.9b, as an example of the simulated exciton rates at a steady state. This is used in Paper II to quantify and compare exciton-exciton and exciton-polaron quenching. The exciton-exciton quenching rate, $k_{\mathrm{SSQ}} \cdot S(x)^2$, described in Chapter 3.4.1, is indicated by the dash-dotted line at the bottom of Figure 4.9b and is barely visible. The $k_{\mathrm{SPQ,p}} \cdot S(x) \cdot p(x)$ and $k_{\mathrm{SPQ,n}} \cdot S(x) \cdot n(x)$ terms are the exciton:electron-polaron and the exciton:hole-polaron quenching rate, described in Chapter 3.4.2, indicated by the dotted lines in Figure 4.9b. In Papers I and II, the steady-state exciton generation rate, the radiative decay rate, the exciton quenching rate in Eq. 4.6 are simulated and later used to analyze the EZ formation and to understand the efficiency roll-off.

5 Novel approaches to improve LEC performance

In this chapter, a number of novel approaches that can be used to improve the LEC performance are presented. In Paper I, the emission efficiency is improved by controlling the EZ position through the inclusion of an appropriate additive into the active material. In Paper II, we find that the efficiency roll-off in a singlet-exciton emitter LEC is primarily caused by exciton-polaron quenching due to the increasing concentration of polarons in the emissive p-n junction region. In Paper III, the EZ width is determined and found to be about 20 % of the active material layer. We also observed that the steady-state EZ width decreases slightly with increasing current density. The findings from Papers II and III give the tools that can facilitate an efficiency improvement by controlling the EZ width in the future.

5.1 Controlling the EZ position through additives

We have seen that the EZ position has a significant impact on the outcoupling efficiency in Chapters 3.5 and 4.4. Therefore, it is crucial to explore methods for controlling the EZ position. Previous attempts to control the EZ have focused on the selection of the OSC by adjusting the electronic mobility ratio. Combining different OSCs has also been shown to be tool for the tuning of the EZ position and/or width.[84, 85] Controlling the EZ has also been achieved through the selection and concentration of mobile ions by adjusting the ionic mobility ratio. A set of ionic liquids with differently sized cations was used to control the EZ position.[86] It has been demonstrated that the ion concentration in the active material controls the steady-state doping concentration and thereby the EZ width.[15, 87] In this Chapter, we demonstrate that the EZ position can be effectively controlled by including an appropriate additive into the active material.

5.1.1 EZ position for two ion-transporters

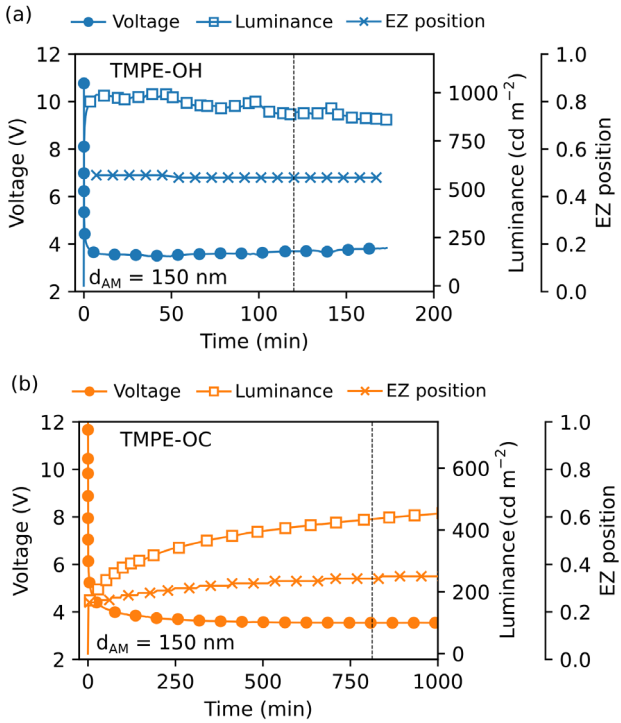

Figure 5.1. The voltage, the forward luminance and the EZ position transients of two types of LEC devices: (a) TMPE-OH LEC and (b) TMPE-OC LEC.[77] The vertical dotted lines indicate the time of steady state.

To assess the impact of adding an additive to the active material, two different star-shaped ion transporter molecules with different end groups, presented in Figure 2.1b, are investigated. Two types of devices are fabricated, as described in Chapter 2.1, and referred to as TMPE-OH LEC and TMPE-OC LEC, based on the ion-transporter being either TMPE-OH or TMPE-OC, respectively.

Figure 5.1 presents the time evolution for the voltage, the forward luminance and the EZ position for the TMPE-OH LEC and the TMPE-OC LEC; the EZ positions are extracted using the conventional spectrogoniometer setup and the simplified optical model. The minimum voltage of these two LECs is similar at 3.5 V, indicating a similar level of doping at steady state. In contrast, the time to reach minimum voltage is significantly longer for the TMPE-OC LEC than the TMPE-OH LEC, showing that the total ion mobility in the active material is lower with the larger TMPE-OC as the ion transporter than the smaller TMPE-OH. The

TMPE-OH LEC exhibits a higher forward luminance by > 100 %, and a higher power efficiency by 60 % compared to the TMPE-OC LEC.

Both the transient and the steady-state EZ position of the two LECs are notably different. For the TMPE-OH LEC, the EZ initially forms close to the center of the active material and is maintained at essentially the same position until steady state is reached. This is in strong contrast to the situation for the TMPE-OC LEC, for which the EZ initially forms close to anode, and then shifts towards the center of the active material. The steady-state EZ position, indicated by the vertical black dotted line, is 0.48 for the TMPE-OH LEC and 0.34 for the TMPE-OC LEC. Thus, the inclusion of the TMPE-OC results in a steady-state EZ located close to the anode, while the addition of the TMPE-OH shifts the steady-state EZ position to the center of the active material. The different EZ behavior results in a different outcoupling efficiency, as shown by the orange solid line in Figure 4.7, which accounts for most of the increased forward luminance and the improved power efficiency of the TMPE-OH LEC compared to the TMPE-OC LEC.

5.1.2 Origin of the differing EZ position behavior

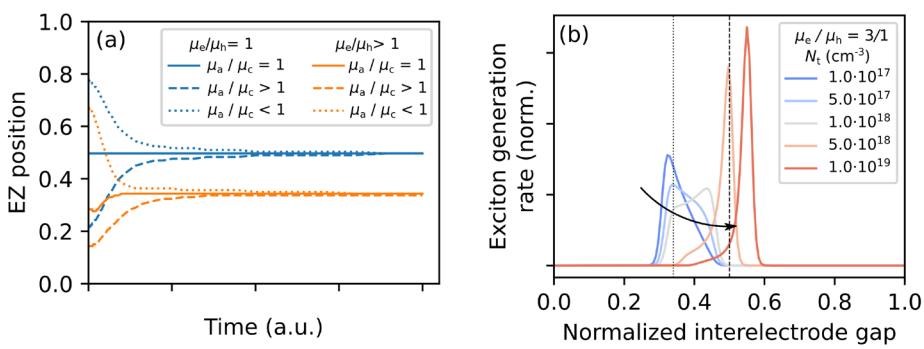

Figure 5.2. The transient evolution of the EZ position and the simulated exciton generation profile with a drift-diffusion model.[77] (a) The transient EZ position with different mobility ratios of the electron (μ_e), hole (μ_h), the anion (μ_a) and the cation (μ_c), as defined in the legend. (b) The exciton generation profile at different electron trap density, N_t, as defined in the inset. The dotted and dashed vertical lines indicate the EZ position at 0.34 and 0.48, respectively.

As described in Chapter 2.3, the ions redistribute upon applying a voltage in an LEC, followed by the transport of the injected electrons and holes through the active material layer. To rationalize our findings of different EZ positions, the drift-diffusion model presented in Chapter 4.5, is used to simulate both the transient and steady-state EZ position of an LEC with

different ionic and electronic mobility ratios. Figure 5.2a displays the simulated EZ position with different mobility ratios between the anions (μ_a) and the cations (μ_c), and different ratios between the mobility of electrons (μ_e) and holes (μ_h). This figure reveals that the ionic mobility ratio determines the initial EZ position, while the electronic mobility ratio determines the steady-state EZ position. Let us see that in more detail.

A μ_a/μ_c ratio larger than 1 results in an initial EZ position closer to the anodic interface at 0, indicated by the dashed lines in Figure 5.2a. This can be conceptually explained by the fact that the higher-mobility (i.e., faster-drifting) anions redistribute quicker than the cations to compensate the oxidized site of OSC and accumulate at a high concentration in a narrower region (i.e., p-type doping region) near the anode. Similarly, the lower-mobility cations accumulate at a lower concentration in a wider region (i.e., n-type doping region), so the initial EZ, between the narrower p-doped and wider n-doped regions, forms close to the anode. The opposite scenario, with a μ_a/μ_c ratio smaller than 1, results in an initial EZ position closer to the cathode, indicated by the dotted lines in Figure 5.2a.

Now, let's examine the effect of the electronic mobility ratio on the EZ position, as indicated by the orange lines in Figure 5.2a. When $\mu_e/\mu_h > 1$, the resulting steady-state EZ position is found closer to the anode. The orange lines, with different ionic mobility ratios, are finally stabilized at the same value, indicating that the ion mobility ratio has no influence on the steady-state EZ position. The opposite scenario, with an μ_e/μ_h ratio smaller than 1, results in a steady-state EZ position closer to the cathode for symmetry reasons. As expected, a μ_e/μ_h ratio equal to 1 results in a steady-state EZ position at the center of the active material layer, as indicated by the blue lines in Figure 5.2a. The described simulation findings on both the initial and the steady-state EZ positions are in agreement with the results presented in Ref.[21].

A comparison with the measured transient EZ position in Figure 5.1 and Figure S2 in Paper I, reveals that the TMPE-OH LEC and the TMPE-OC LEC perform like the dotted blue line ($\mu_a/\mu_c < 1$; $\mu_e/\mu_h = 1$) and the dashed orange line ($\mu_a/\mu_c > 1$; $\mu_e/\mu_h > 1$), respectively. The initial EZ positions vary with different ion-transporters, indicating that the ionic mobility is influenced differently depending on the ion-transporter. Moreover, the steady-state EZ position with different ion-transporters is also different. This observation is not at first expected, since the emitter remains the same for all types of LECs and since the simulation results in

Figure 5.2 indicate that the steady-state EZ position is solely determined by the electron/hole mobility of the emitter.

To clarify the origin of the observed shift in the steady-state EZ position from TMPE-OC LEC to TMPE-OH LEC, Figure 5.2b shows that by introducing electron traps,[38] a similar shift can be achieved. As the electron trap density, N_t, increases from $1{\cdot}10^{17}$ cm^{-3} to $5{\cdot}10^{18}$ cm^{-3}, the resulting EZ position shift closely matches the measured shift from 0.34 to 0.48, as indicated by the dotted and dashed vertical lines in Figure 5.2b, respectively. In line with the simulations, we speculate that the addition of the smaller, more polar, hydrogen-bonding TMPE-OH ion-transporter induces charge-trapping and/or hydrogen-bonding interactions with SY, resulting in a lower electron transport capacity of SY film. Additional experiments and further discussion can be found in Paper I.

5.1.3 Controlled EZ position

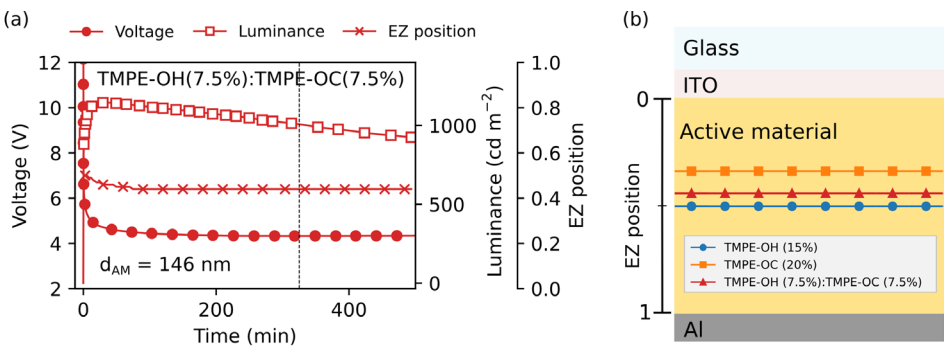

Figure 5.3. (a) The temporal evolution of the voltage (filled circles), the forward luminance (open squares) and the EZ position (crosses) for a TMPE-OH/OC-blend LEC.[77] (b) A schematic of LEC devices with controlled EZ positions at steady state, achieved by tuning the mass ratio (indicated in the legend) of the ion transporters.

To verify whether the ion-transporter additive affects the light-emission behavior, a combination of the two ion-transporters (TMPE-OH:TMPE-OC=1:1) is used to fabricate a third device type. The measured voltage, forward luminance, and the extracted EZ position for a TMPE-OH/OC-blend LEC is presented in Figure 5.3a, with a steady-state EZ position of 0.44, indicated by the vertical black dashed line. Figure 5.3b illustrates the EZ position at steady state in an LEC device for the different ion-transporters studied. A combination of the two ion-transporters does result in an intermediate EZ position of the single ion-transporter TMPE-OH LEC and TMPE-OC LEC, revealing that the EZ position can be

effectively controlled by tuning the additives in the active material. By increasing the ratio of TMPE-OH additive in the active material, the EZ position moves closer to the center of the active material layer resulting in a higher emission efficiency.

5.2 Understanding the efficiency roll-off

The LEC emission efficiency was improved by controlling the EZ position at one fixed constant current density in Chapter 5.1. However, a common observation in both LECs[84, 88-92] and OLEDs[93-96] is that the emission efficiency drops with increasing current, an effect commonly termed as efficiency roll-off. In Chapter 3, we analyzed the EQE equation and showed that two critical factors are the exciton losses and the outcoupling efficiency. As we have just shown, the latter is strongly dependent on the EZ position, suggesting that the internal loss mechanisms only can be investigated and understood after removing the influence of the outcoupling efficiency.

In this chapter, to properly address the roll-off in LECs, we first disentangle the outcoupling efficiency due to the microcavity effect by measuring the EZ position as a function of current density. After quantifying the outcoupling efficiency using the procedure described in Chapter 4, the major exciton loss factors of LEC devices are separated and quantified using the procedure described in Chapter 3.

5.2.1 LEC performance at different current densities

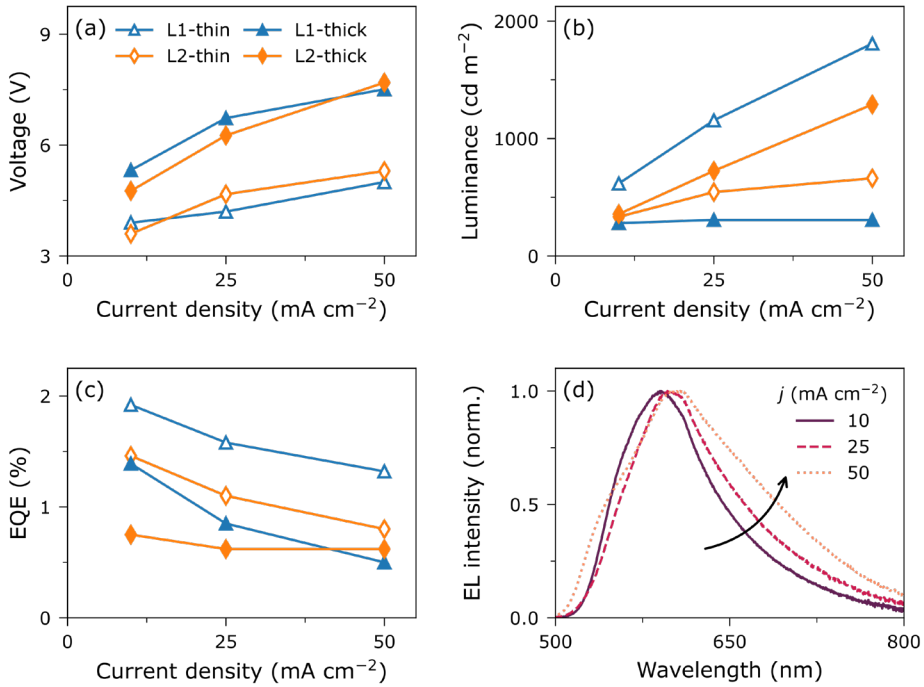

Figure 5.4. The steady-state (a) voltage, (b) forward luminance and (c) EQE of L1-thin, L1-thick, L2-thin and L2-thick LEC. (d) The forward EL spectra of L1-thick LEC at steady state at three different current densities, identified in the inset. The spectral shift with increasing current density is indicated by the black arrow.

We investigate four types of devices, termed L1-thin (TMPE-OH LEC, 180 nm), L1-thick (TMPE-OH LEC, 400 nm), L2-thin (TMPE-OC LEC, 130 nm) and L2-thick (TMPE-OC LEC, 260 nm). The motivation for this selection of different ion-transporters and thicknesses of the active material is that they result in different EZ positions, and thus different outcoupling efficiencies, as shown in Chapters 4.4 and 5.1.1. The performance of these LEC devices at three different constant current densities, 10, 25 and 50 mA cm^{-2}, are measured using the conventional spectrogoniometer setup and fitted with the simplified optical model. We focus on the performance at steady state, defined as the point at which the minimum voltage is reached.

The steady-state performance of the four LECs is shown in Figure 5.4. The steady-state voltage in Figure 5.4a increases with both increasing current density and increasing thickness of the active material, as expected. The

steady-state forward luminance, in Figure 5.4b, exhibits the expected increase with increasing current density for most LECs. Curiously, the luminance of L1-thick shows no notable increase despite a doubling of the current density from 25 to 50 mA cm^{-2}. The steady-state EQE, presented in Figure 5.4c, decreases with increasing current density; that is the effect commonly referred to as efficiency roll-off. Here, the L1-thick shows a 64 % decrease in EQE from 10 to 50 mA cm^{-2}, while surprisingly the change for L2-thick is much smaller, and essentially zero at the higher current densities. The steady-state forward EL spectra of L1-thick as a function of current density is presented in Figure 5.4d, and it is found that the EL spectra redshifts and that the full width at half maximum of the EL spectra increases as the current density increases. These changes in EL spectra indicate a shifting EZ position with changing current density.

5.2.2 Extracted EZ position and outcoupling efficiency

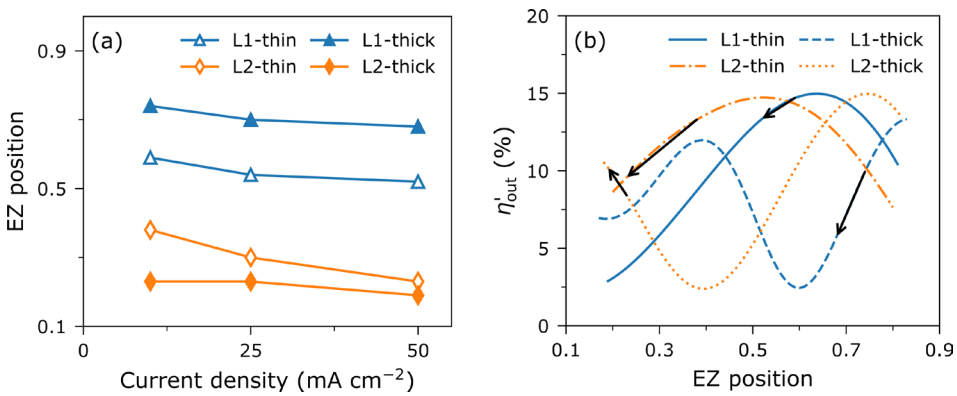

Figure 5.5. (a) The extracted steady-state EZ position as a function of current density for the four LECs. (b) The simulated effective outcoupling efficiency. The black arrows indicate the changes in the outcoupling efficiency that result from the observed shift of the EZ position shown in Figure (a) with increasing current density.

The drastically different behavior in the luminance and the EQE with current density for the four LECs can result from different microcavity effects, i.e. outcoupling. Therefore, we investigate the EZ position using the same conventional spectrogoniometer setup and simplified optical model as in Paper I. The steady-state EZ position, presented in Figure 5.5a, shifts toward the anode with increasing current density for all four LECs. As shown in Chapter 5.1.2, the steady-state EZ position is determined by the electron/hole mobility ratio, with $\mu_e/\mu_h > 1$ resulting in a steady-state EZ position closer to the anode. Therefore, the anodic shift of the steady-state EZ position with increasing current density can

result from a greater increase of the electron mobility than the hole mobility with increasing electric field.[97] We speculate that this asymmetric change in mobility can be caused by that the depth of the electron traps are deeper than that of the hole traps.[98, 99]

The observed EZ position shift with increasing current density is important for the analysis of the emission efficiency, since the outcoupling efficiency, and consequently EQE, can be affected significantly. The optical simulation described in Chapter 4.2, using the estimated EZ width from Ref.[25], is performed to derive the corresponding outcoupling efficiency as a function of EZ position, shown in Figure 5.5b. The pronounced undulating behavior of the outcoupling efficiency, particularly in the thick LECs, is a clear manifestation of the interference effect in the microcavity, as described in Chapter 3.5.3. The black arrows indicate the changes in the outcoupling efficiency that result from the observed shift of the EZ position (see Figure 5.5a) with increasing current density from 10 to 50 mA cm^{-2} for the four LEC devices. The outcoupling efficiency of L1-thick (dashed blue line) drops by 42 %, while it in contrast increases by 21 % for L2-thick (dotted orange line).

5.2.3 Derived and simulated exciton losses

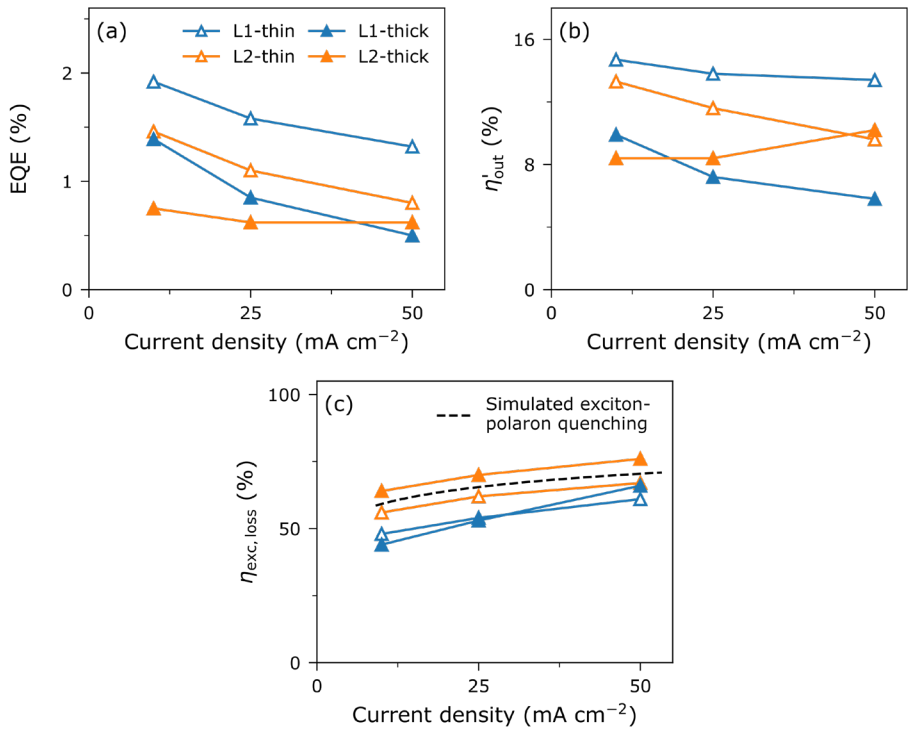

Figure 5.6. (a) The measured EQE as a function of current density for all LECs using the conventional spectrogoniometer setup. (b) The simulated effective outcoupling efficiency at steady state. (c) The extracted exciton loss factor using the measured EQE and simulated outcoupling efficiency. The dashed black line represents the simulated exciton-polaron quenching.

The measured values for the steady-state EQE as a function of current density for all LECs using the conventional spectrogoniometer setup are presented in Figure 5.6a. The previously simulated values for the effective outcoupling efficiency at steady state are summarized in Figure 5.6b. By inserting these values in Eq. 3.1, the exciton loss factor ($\eta_{exc,loss}$) described in Chapter 3.4 can be calculated and the results for the four LECs are displayed in Figure 5.6c. The four derived traces show that the internal loss factors of the four devices are quite similar. We also note that exciton loss factor is high at 44-64 % even at the relatively low current density of 10 mA cm^{-2} and that it significantly increase to 61-76 % with increasing current density to 50 mA cm^{-2}. This shows that a major contributor to the efficiency roll-off of these LEC devices is exciton loss.

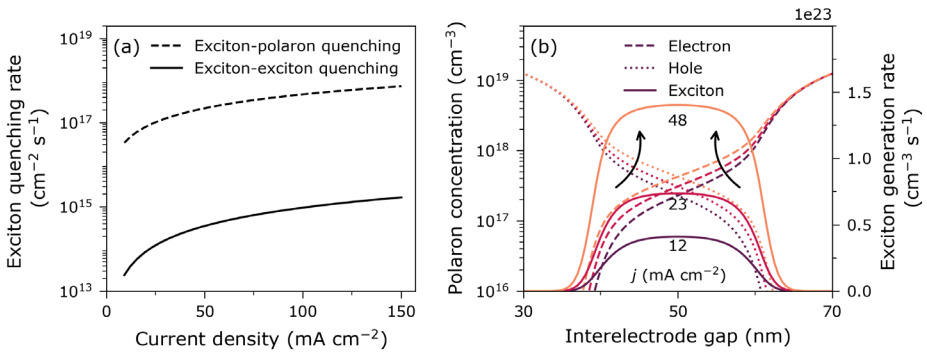

Figure 5.7. (a) The simulated exciton quenching rates as a function of current density: exciton-exciton quenching (solid line) and exciton-polaron quenching (dashed line). (b) The simulated electron-polaron (dashed lines) and hole-polaron (dotted lines) concentration and exciton generation rates (solid lines) with increasing current densities.

For a more detailed analysis of these exciton losses, we use the electrical drift-diffusion model, as presented in Chapter 4.5, to simulate the different loss channels of the emissive singlet excitons. Here, we only consider the exciton-exciton and exciton-polaron quenching processes, whose derived rates as a function of current density are presented in Figure 5.7a. The exciton-exciton quenching is much lower, by two orders of magnitude, than the exciton-polaron quenching, which is due to the short lifetime of the emissive singlets in SY. The exciton-polaron quenching, indicated by the black dashed line in Figure 5.6c, replicates the trend of the calculated exciton loss traces for all four LECs. These results thus imply that exciton-polaron quenching is the dominant exciton loss process in the four investigated singlet-emitting LECs.

The reason for the increase of exciton-polaron quenching with increasing current density is revealed in Figure 5.7b, which presents the simulated polaron profiles and the exciton generation rate at three different current densities. The simulated polaron concentration in the p-n junction region, i.e., the exciton generation region, increases with increasing current density, so the exciton-polaron quenching increases with increasing current density. The reason for the observed high exciton loss even at the relatively low current density of 10 mA cm^{-2} is the LEC-characteristic high electrochemical-doping concentration and the concomitant high polaron concentration.

5.3 Determining the dynamic emission zone

The EZ width has a strong influence on the LEC performance, since the EZ is both the most resistive region and the place where exciton losses originate in an LEC. The challenge is that it is difficult to experimentally determine the width of the dynamic EZ in thin sandwich-cell LECs. In this chapter, we address this issue by using the refined spectrogoniometer setup and the advanced optical model, as described in Chapters 4.1.2, 4.2.2, and the corresponding fitting process described in Chapter 4.3.2 to extract the transient and steady-state EZ width at different current densities.

5.3.1 Transient EZ

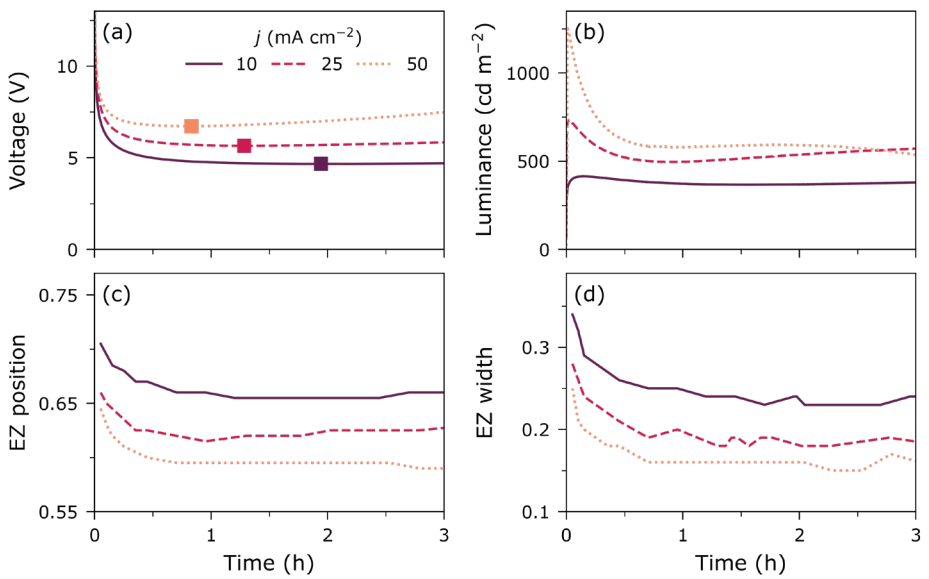

Figure 5.8. The transient (a) voltage, (b) forward luminance, (c) EZ position and (d) EZ width for a TMPE-OH LEC device driven by a constant current density of 10, 25 or 50 mA cm⁻², as identified in the legend of (a). The solid squares in (a) indicate the time to reach minimum voltage, i.e. steady state.

We first present the transient performance of a TMPE-OH LEC during the first 3 h of operation. Figure 5.8a-b displays the transient voltage and forward luminance, respectively, for three different current densities of 10, 25 and 50 mA cm⁻², as identified in the inset of Figure 5.8a. The voltage drops rapidly during the initial operation (< 3 min), and reaches the minimum voltage at the time indicated by the square markers in Figure 5.8a; the initial transient decrease of the voltage during constant-current

operation is a characteristic feature of a well-functioning LEC. The forward luminance, as presented in Figure 5.8b, increases rapidly during the initial operation, which is in line with the formation of EDLs and electrochemical doping, as described in Chapter 2.3.

Figure 5.8c-d displays the best-fit transient EZ position and width, respectively. We note that the EZ position and width cannot be measured with the same high time resolution as the voltage and the forward luminance, since each data set of angle-resolved EL spectra using the refined spectrogoniometer setup, as presented in Chapter 4.1.2, needs more than 1 min to record at all angles. The fitting procedure assumes an unchanged EZ structure throughout the entire duration of the measurement, which is not true during the first 3 min of LEC operation where the luminance is drastically changing from the beginning to the end of each data set. The transient EZ position and width are therefore not shown for t < 3 min. For t > 3 min, the temporal change in luminance is low enough to collect reliable angle-resolved EL data.

The EZ position, presented in Figure 5.8c, forms closer to the cathode at 0.65-0.70, and then moves towards the center of the active material layer. The entire EZ position transient is observed to shift towards the anode with increasing current density. The EZ width, as presented in Figure 5.8d, is observed to decrease during the initial LEC operation and the entire EZ width transient appears to narrow with increasing current density.

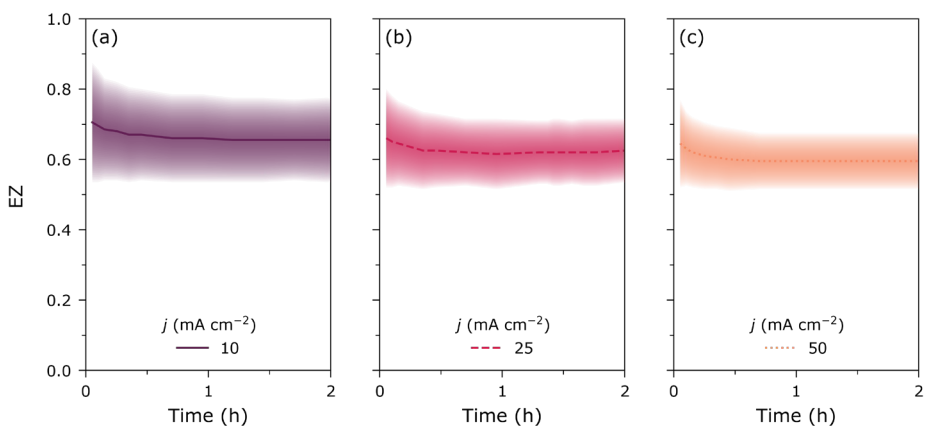

Figure 5.9. The extracted temporal evolution of the EZ at different current densities of (a) 10, (b) 25 and (c) 50 mA cm⁻². The EZ position and width are indicated by the thick line and the shaded area, respectively.

Now, we can combine the extracted EZ position (thick line) and the EZ width (shaded area) to visualize the temporal evolution of the dynamic EZ in plots such as Figure 5.9a-c. The EZ width continues to decrease after the initial operation, indicating that electrochemical doping processes are still ongoing, i.e., that the overall doping concentration increases and the p-n junction is thinning. Subsequently, the EZ position and width are stable, indicating that the device has reached steady state. The transient behavior of the EZ width during the first 2 h is similar to the trend simulated by drift-diffusion modelling[21] and impedance spectroscopy.[100, 101]

5.3.2 Steady-state EZ

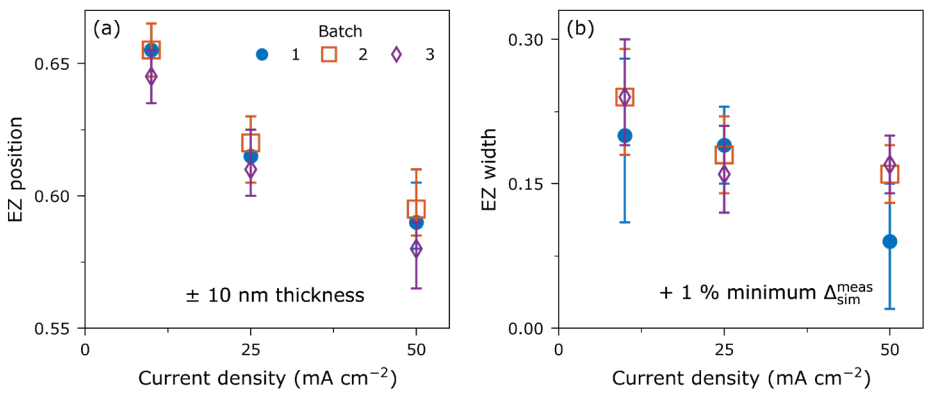

Figure 5.10. (a) The steady-state EZ position with the error bars indicating a ± 10 nm change in the active material thickness. (b) The steady-state EZ width with the error bars indicating a 1 % increase of the minimum error. Data for three different LEC batches are presented.

To investigate repeatability, we fabricated and measured three batches of TMPE-OH LECs. Each batch consists of three devices operated at three different current densities. The steady-state EZ position and the steady-state EZ width as a function of the current density for the three batches are presented in Figure 5.10a and b, respectively. Batch 1, 2, and 3 are indicated by the blue circles, orange squares and purple diamonds, respectively. The error bars are derived from the "worst" uncertainty factor, i.e., ± 10 nm variation of the active-material thickness for the EZ position, and a + 1 % variation of the minimum Δ_{sim}^{meas} for the EZ width, as gleaned from Figure S3 in Paper III. The steady-state EZ position is invariably observed to shift towards the anode with increasing current density, confirming the trend obtained with the conventional spectrogoniometer setup and simplified optical model presented in Figure

5.5a. The steady-state EZ width is found to be ~20 % of the active material film thickness at 10 mA cm^{-2} operation and appears to be decreasing with increasing current density.

The indication that the steady-state EZ width decreases with increasing current density is in line with earlier studies using impedance spectroscopy.[22, 24, 102] We note that the EZ width was assumed constant with current density for the determination of the outcoupling efficiency in Paper II, while in Paper III it was found to vary with current density. This current-density dependent outcoupling efficiency could now be used for a more accurate analysis of efficiency roll-off, as presented in Paper II.

5.4 Electrode-dependent LEC performance

As we saw in Paper I, the performance of LECs can be tuned by including an additive into the active material. In Paper IV, we shift our focus to the electrode material instead, and more specifically, the cathode.

In the LEC community, the electrode material selection is often considered non-critical to the LEC performance due to the *in situ* formation of the EDLs.[103-105] However, the study performed in Paper IV shows that this understanding needs to be modified. Specifically, we show that the electrode work functions can influence the EZ position. For a 180 nm thick TMPE-OH LEC using either Ca, Al or Ag as the cathode material, we found the steady-state EZ position at 0.40, 0.47 and 0.54, respectively, when operated with the same 25 mA cm^{-2} current density. To explain this finding, we propose that the ion concentration in the injection-facilitating EDLs is influenced by the difference between the electrode work function and the corresponding semiconductor orbital (LUMO in this case, as we focus on the cathode selection). This difference in consumed ion concentration in the EDLs in turn affects the number of ions available for electrochemical doping, which consequently shifts the EZ position due to unbalanced p- and n-type doping regions. These findings provide an additional design criterion for optimizing LEC performance by taking the electrode material into consideration.

5.5 Understanding the steady-state ion profile

In Paper II, we used drift-diffusion modeling to understand the exciton losses at steady state, and we realized that: (i) a drift-diffusion modeling is a powerful tool to understand the LEC operational mechanism, and (ii) the shape of the doping profile (i.e., the profile of the ion-compensated

polarons) plays a significant role for the device efficiency via exciton-polaron quenching. However, the steady-state doping profiles were modeled with constant and symmetric gradients for all current densities for simplicity. In Paper V, we replace these ad hoc ion profiles with the profiles resulting from the inclusion of mobile ions into the numerical drift-diffusion model.

The advantage of including mobile ions into the model is that the ion profiles will now need to fulfill their own drift-diffusion equations (one set for the cations and one for the anions). As a result, the ion profiles will depend on the driving conditions since, for example, a change in voltage would lead to a change in the drift pull that the ions are submitted to, as shown in Figure 5.11a. To corroborate this new electrical model, we measured the steady-state current density-voltage curve (*j-V* curve) of a TMPE-OH LEC and compared it with the simulated one (see Figure 5.11b, star symbols versus dashed line). In short, we find that the inclusion of mobile ions into the model is not enough to replicate the experimental *j-V* curve, and that a voltage-dependent mobile ion density needs to be included to replicate it. That is, an increasing/decreasing doping concentration as the voltage increases/decreases. When doing so, the *j-V* curve of the experimental LEC can be well-replicated in simulations, as shown in Figure 5.11b.

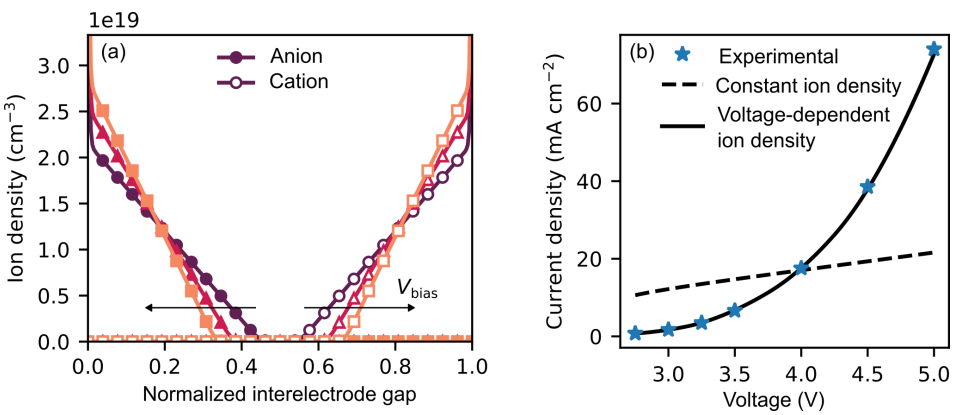

Figure 5.11. (a) Ion density profiles for a mobile ion model (anion, closed symbols and cations open symbols) for three different voltages. (b) The experimental j-V curve of a TMPE-OH LEC (star symbols) compared with the simulated curves when including mobile ions into the simulation for two cases: (i) a constant total ion density case (dashed line), and (ii) total ion density that increases with voltage (solid line).

This finding indicates that the assumption of a constant doping concentration independent on the current density, as used in the

advanced optical model, needs to be revisited and improved. For example, it can be used to define a more accurate optical model with regards to the optical properties of the doped active material layers. This finding also provides an additional possible explanation for the efficiency roll-off observed in Figure 5.4c, as an increasing doping concentration with increasing current density will lead to stronger exciton-polaron quenching.

In the future, it is motivated to further improve the dynamic EZ characterization method so that the EZ width can be determined with higher accuracy. The simulation can be improved by including voltage-dependent doping concentrations, by better replicating the true exciton-generation profiles, and by accounting for the emitter birefringence.[26] The accuracy of the measurement procedure can be improved by increasing the distance between the LEC device and the detector (thus rendering the LEC more akin to a point source), by inserting additional lenses in front of the detector to collect more light,[106] and by reducing the thickness variation of the active material layer.

6 Conclusions

In this thesis, we present and utilize a method for the *in situ* determination of the dynamic EZ in an LEC. The EZ is essentially extracted by comparing the measured and the simulated angle-resolved EL spectra and intensity. The experimental data are measured by a spectrogoniometer setup, and the simulated data are derived from an optical model based on the transfer-matrix formalism.

In Paper I, we show that the EZ position can be shifted from close to the anode towards the centre of the active material layer through the inclusion of an appropriate additive into the active material, and that this shift can result in a 60 % improvement of the emission efficiency. In Paper II, we quantify the light outcoupling efficiency with the aid of the determined EZ position and use this information for the quantification of losses due to exciton quenching. We find that the efficiency roll-off in a common singlet-exciton emitting LEC is mainly due to singlet-exciton:polaron quenching. In Paper III, the first simplified EZ determination method is improved by considering the doping-dependent refractive index of the emitter material, by enhancing the emission intensity using a half-cylinder lens, and by removing the influence of the emitter's anisotropy by the inclusion of a linear polarizer that enables for the selective detection of the s-polarized light. This refined method can be used to extract the transient evolution of both the EZ position and the EZ width in LEC devices. With the refined method, we find that the EZ width initially decreases with time, and that the steady-state EZ width is ~20 % of the active material layer for a common conjugated-polymer LEC. This method development and implementation has thus resulted in a better understanding of the complicated operational mechanism of LECs, and established guidelines for how to control the EZ in LECs for improved emission efficiency.

Contributions

A brief description of my contributions to the papers included in this thesis is as follows:

I. Controlling the Emission Zone by Additives for Improved Light-Emitting Electrochemical Cells
I confirmed the setup by collecting and analyzing experimental data with the support of the co-authors, and participated in the manuscript revision.

II. Efficiency Roll-Off in Light-Emitting Electrochemical Cells
I managed the project, collected and analyzed experimental data, analyzed simulation data with the support of the co-authors, and wrote the manuscript with support of the co-authors.

III. Determining the Dynamic Emission Zone Width in Light-Emitting Electrochemical Cells
I managed the project, collected and analyzed experimental data, and wrote the manuscript with support of the co-authors.

IV. Impact of the Electrode Material on the Performance of Light-Emitting Electrochemical Cells
I measured and analyzed a small portion of the experimental data, and participated in the discussion and revision of the manuscript.

A brief description of my contributions to the manuscript not included in this thesis:

V. Pinpointing the Dynamic pin Junction
I measured and analyzed parts of the experimental data, and participated in the discussion and revision of the manuscript.

Acknowledgement

First, I would like to express my gratitude to my supervisor, Ludvig. I am sincerely grateful for the opportunity to pursue my PhD. I deeply appreciate your supervision and effort, which have guided my work toward publication in a highly regarded journal. Thank you for your invaluable input on my thesis and for your suggestions and support during moments of anxiety. I am especially grateful for your "three-sentence" rule, which has helped me craft a clearer and more focused narrative in the manuscript. Your high expectations have challenged me to grow both academically and personally, shaping me into a stronger and more capable researcher. I also want to extend my heartfelt thanks to my co-supervisor, Christian. I am deeply grateful for your patient supervision and guidance. With your support, I have learned to communicate more effectively and express myself with greater clarity. I truly appreciate and enjoy our deep discussions and the moments of inspiration you have provided. Your strong enthusiasm and high standards have had a profound influence on me. I also sincerely appreciate the time and effort you have dedicated to my work, even on some weekends. I also want to thank my co-supervisor, Thomas, and my reference person, Ove. Your support and guidance have helped keep my PhD progress on the right track.

I would extend my thanks to OPEG members: Jia, you are my "mental supervisor". Thanks for keeping me company and explaining things when I felt upset and confused from a different perspective. Your kindness re-energized me and gave me the strength to face the challenges of my PhD. I also appreciate your guidance in working as a lab supervisor. Joan, although you are not officially my supervisor, you teach me a lot about simulation and Python with your detailed explanation. You guided me to improve my writing skills, a crucial aspect of my PhD journey. Shi, I am deeply grateful for your detailed guidance on fabricating well-functioning LECs, which formed the foundation of my entire PhD work. Roushdey, thank you so much for your invaluable support in the instruction, repair, and maintenance of the lab equipment. Junkai and Menghong family, thanks for taking care of me when I was sick and for the joy that little and adorable Chris brought into my life. Your kindness and warmth meant so much to me. I am truly grateful to Junkai for sharing his skills on Endnote. So-Ra, thank you for the wonderful weekends filled with delicious food and gatherings with your friends. Those moments were truly enjoyable and memorable. Anton, thank you for inviting me to your home and for the wonderful evenings spent enjoying delicious dinners and experiencing

traditional culture. Etienne and Sandra, I truly appreciate you for sharing your experiences about PhD studies. Thushar, thanks for your help in modify the plotting. Yuntao, thank you for the insightful research discussions and for sharing delicious lunches with me when I was busy with my thesis. I also appreciate Mattias, Andreas, Petter, Yongfeng, Jenny, Gunel, Sandra, Henry, Jean Claude, Kumar, William, and Sikha for the valuable research discussions.

I would like to express my deepest gratitude to everyone from the department of Physics who has supported me throughout my academic journey. A special thanks to Katarina for your immense help with my residence permit and contract. Your guidance and patience made these complex processes much smoother. Thanks to Laszlo for your help with the defense application and registration documents. Thanks to Gabriella for your assistance in booking rooms. Thanks to Sussie for maintaining a clean work environment. Thanks to Jorgen for always fixing any access and card issues.

Last but not least, I express my heartfelt gratitude to my family for their unwavering financial and emotional support. Your encouragement has been my foundation and motivation, and I am forever grateful for your belief in me. I feel incredibly fortunate to be your daughter and younger sister, wrapped in your deep love. You are my greatest source of strength and my warmest refuge. Da, thank you for your incredible encouragement, boundless forgiveness, and unwavering support throughout my PhD journey, especially during the extremely busy times. To Yuyan and Xingming, my teachers and friends, I am immensely grateful for your financial and emotional support during my master's program. Your kindness and generosity helped me navigate challenging times, and I cannot thank you enough for your trust and care. I want to express my deepest gratitude to Professor Tiancai Zhang. I am incredibly thankful for your kind assistance during the final year of my bachelor's program, one of the most challenging periods of my life. I also sincerely appreciate the information you provided about open PhD positions. Thank you for bringing sunshine into my life. To the REALab, thanks for providing me with practical training and hands-on experience in experimental physics, which has deeply motivated me to continue my studies and pursue research. I also extend my sincere thanks to Shanxi University for the scholarship that supported my exchange program, which greatly enriched both my academic and personal growth.

References

1. Pei, Q.; Yu, G.; Zhang, C.; Yang, Y.; Heeger, A. J., Polymer Light-Emitting Electrochemical Cells. *Science* **1995,** *269* (5227), 1086-1088.
2. Cao, Y.; Yu, G.; Heeger, A. J.; Yang, C. Y., Efficient, fast response light-emitting electrochemical cells: Electroluminescent and solid electrolyte polymers with interpenetrating network morphology. *Applied Physics Letters* **1996,** *68* (23), 3218-3220.
3. Pei, Q.; Yang, Y.; Yu, G.; Zhang, C.; Heeger, A. J., Polymer Light-Emitting Electrochemical Cells: In Situ Formation of a Light-Emitting p−n Junction. *Journal of the American Chemical Society* **1996,** *118* (16), 3922-3929.
4. Sandström, A.; Dam, H. F.; Krebs, F. C.; Edman, L., Ambient fabrication of flexible and large-area organic light-emitting devices using slot-die coating. *Nature Communications* **2012,** *3* (1), 1002.
5. Auroux, E.; Huseynova, G.; Ràfols-Ribé, J.; Miranda La Hera, V.; Edman, L., A metal-free and transparent light-emitting device by sequential spray-coating fabrication of all layers including PEDOT:PSS for both electrodes. *RSC Advances* **2023,** *13* (25), 16943-16951.
6. Ren, J.; Opoku, H.; Tang, S.; Edman, L.; Wang, J., Carbon Dots: A Review with Focus on Sustainability. *Advanced Science* **2024,** *11* (35), 2405472.
7. Liu, Y.; Tang, S.; Wu, X.; Boulanger, N.; Gracia-Espino, E.; Wågberg, T.; Edman, L.; Wang, J., Carbon nanodots: A metal-free, easy-to-synthesize, and benign emitter for light-emitting electrochemical cells. *Nano Research* **2022,** *15* (6), 5610-5618.
8. Sandström, A.; Edman, L., Towards High-Throughput Coating and Printing of Light-Emitting Electrochemical Cells: A Review and Cost Analysis of Current and Future Methods. *Energy Technology* **2015,** *3* (4), 329-339.
9. Zimmermann, J.; Porcarelli, L.; Rödlmeier, T.; Sanchez-Sanchez, A.; Mecerreyes, D.; Hernandez-Sosa, G., Fully Printed Light-Emitting Electrochemical Cells Utilizing Biocompatible Materials. *Advanced Functional Materials* **2018,** *28* (24), 1705795.
10. Zimmermann, J.; Schlisske, S.; Held, M.; Tisserant, J.-N.; Porcarelli, L.; Sanchez-Sanchez, A.; Mecerreyes, D.; Hernandez-Sosa, G., Ultrathin Fully Printed Light-Emitting Electrochemical Cells with Arbitrary Designs on Biocompatible Substrates. *Advanced Materials Technologies* **2019,** *4* (3), 1800641.
11. Dick, D. J.; Heeger, A. J.; Yang, Y.; Pei, Q., Imaging the structure of the p-n junction in polymer light-emitting electrochemical cells. *Advanced Materials* **1996,** *8* (12), 985-987.

12. Gao, J.; Dane, J., Planar polymer light-emitting electrochemical cells with extremely large interelectrode spacing. *Applied Physics Letters* **2003,** *83* (15), 3027-3029.
13. Matyba, P.; Maturova, K.; Kemerink, M.; Robinson, N. D.; Edman, L., The dynamic organic p–n junction. *Nature Materials* **2009,** *8* (8), 672-676.
14. van Reenen, S.; Matyba, P.; Dzwilewski, A.; Janssen, R. A. J.; Edman, L.; Kemerink, M., A Unifying Model for the Operation of Light-Emitting Electrochemical Cells. *Journal of the American Chemical Society* **2010,** *132* (39), 13776-13781.
15. Fang, J.; Yang, Y.; Edman, L., Understanding the operation of light-emitting electrochemical cells. *Applied Physics Letters* **2008,** *93* (6).
16. Wågberg, T.; Hania, P. R.; Robinson, N. D.; Shin, J.-H.; Matyba, P.; Edman, L., On the Limited Operational Lifetime of Light-Emitting Electrochemical Cells. *Advanced Materials* **2008,** *20* (9), 1744-1749.
17. Hohertz, D.; Gao, J., How Electrode Work Function Affects Doping and Electroluminescence of Polymer Light-Emitting Electrochemical Cells. *Advanced Materials* **2008,** *20* (17), 3298-3302.
18. Shin, J.-H.; Robinson, N. D.; Xiao, S.; Edman, L., Polymer Light-Emitting Electrochemical Cells: Doping Concentration, Emission-Zone Position, and Turn-On Time. *Advanced Functional Materials* **2007,** *17* (11), 1807-1813.
19. Edman, L.; Pauchard, M.; Liu, B.; Bazan, G.; Moses, D.; Heeger, A. J., Single-component light-emitting electrochemical cell with improved stability. *Applied Physics Letters* **2003,** *82* (22), 3961-3963.
20. Adachi, C.; Tokito, S.; Tsutsui, T.; Saito, S., Electroluminescence in Organic Films with Three-Layer Structure. *Japanese Journal of Applied Physics* **1988,** *27* (2A), L269.
21. Diethelm, M.; Schiller, A.; Kawecki, M.; Devižis, A.; Blülle, B.; Jenatsch, S.; Knapp, E.; Grossmann, Q.; Ruhstaller, B.; Nüesch, F.; Hany, R., The Dynamic Emission Zone in Sandwich Polymer Light-Emitting Electrochemical Cells. *Advanced Functional Materials* **2020,** *30* (33), 1906803.
22. van Reenen, S.; Janssen, R. A. J.; Kemerink, M., Dynamic Processes in Sandwich Polymer Light-Emitting Electrochemical Cells. *Advanced Functional Materials* **2012,** *22* (21), 4547-4556.
23. van Reenen, S.; Janssen, R. A. J.; Kemerink, M., Doping dynamics in light-emitting electrochemical cells. *Organic Electronics* **2011,** *12* (10), 1746-1753.
24. Munar, A.; Sandström, A.; Tang, S.; Edman, L., Shedding Light on the Operation of Polymer Light-Emitting Electrochemical Cells Using Impedance Spectroscopy. *Advanced Functional Materials* **2012,** *22* (7), 1511-1517.

25. Lindh, E. M.; Lundberg, P.; Lanz, T.; Edman, L., Optical analysis of light-emitting electrochemical cells. *Scientific Reports* **2019,** *9* (1), 10433.
26. Ràfols-Ribé, J.; Hänisch, C.; Larsen, C.; Reineke, S.; Edman, L., In Situ Determination of the Orientation of the Emissive Dipoles in Light-Emitting Electrochemical Cells. *Advanced Materials Technologies* **2023,** *8* (13), 2202120.
27. Tang, S.; Edman, L., Quest for an Appropriate Electrolyte for High-Performance Light-Emitting Electrochemical Cells. *The Journal of Physical Chemistry Letters* **2010,** *1* (18), 2727-2732.
28. Hofmann, S.; Thomschke, M.; Lüssem, B.; Leo, K., Top-emitting organic light-emitting diodes. *Optics Express* **2011,** *19* (S6), A1250-A1264.
29. Auroux, E.; Park, S.-R.; Ràfols-Ribé, J.; Edman, L., Ion transfer into solution-processed electrodes can significantly shift the p–n junction and emission efficiency of light-emitting electrochemical cells. *Applied Physics Letters* **2022,** *121* (23).
30. Burroughes, J. H.; Bradley, D. D. C.; Brown, A. R.; Marks, R. N.; Mackay, K.; Friend, R. H.; Burns, P. L.; Holmes, A. B., Light-emitting diodes based on conjugated polymers. *Nature* **1990,** *347* (6293), 539-541.
31. Larsen, C. Fabricating designed fullerene nanostructures for functional electronic devices. Umeå universitet, 2014.
32. Köhler, A.; Bässler, H., Triplet states in organic semiconductors. *Materials Science and Engineering: R: Reports* **2009,** *66* (4), 71-109.
33. Charges and Excited States in Organic Semiconductors. In *Electronic Processes in Organic Semiconductors*, 2015; pp 87-191.
34. Kokil, A.; Yang, K.; Kumar, J., Techniques for characterization of charge carrier mobility in organic semiconductors. *Journal of Polymer Science Part B: Polymer Physics* **2012,** *50* (15), 1130-1144.
35. Auroux, E. Solution-processed light-emitting electrochemical cells: challenges and opportunities. Umeå University, 2023.
36. Scaccabarozzi, A. D.; Basu, A.; Aniés, F.; Liu, J.; Zapata-Arteaga, O.; Warren, R.; Firdaus, Y.; Nugraha, M. I.; Lin, Y.; Campoy-Quiles, M.; Koch, N.; Müller, C.; Tsetseris, L.; Heeney, M.; Anthopoulos, T. D., Doping Approaches for Organic Semiconductors. *Chemical Reviews* **2022,** *122* (4), 4420-4492.
37. The Electronic Structure of Organic Semiconductors. In *Electronic Processes in Organic Semiconductors*, 2015; pp 1-86.
38. Electronic and Optical Processes of Organic Semiconductors. In *Electronic Processes in Organic Semiconductors*, 2015; pp 193-305.
39. Tang, S.; Mindemark, J.; Araujo, C. M. G.; Brandell, D.; Edman, L., Identifying Key Properties of Electrolytes for Light-Emitting Electrochemical Cells. *Chemistry of Materials* **2014,** *26* (17), 5083-5088.

40. Fundamentals of Organic Semiconductor Devices. In *Electronic Processes in Organic Semiconductors*, 2015; pp 307-388.
41. Lundberg, P. Light for a brighter morrow: paving the way for sustainable light-emitting devices. Umeå universitet, 2020.
42. Lindh, E. M. On the operation of light-emitting electrochemical cells. Umeå Universitet, 2019.
43. Forrest, S. R.; Bradley, D. D. C.; Thompson, M. E., Measuring the Efficiency of Organic Light-Emitting Devices. *Advanced Materials* **2003,** *15* (13), 1043-1048.
44. Kim, J.-S.; Ho, P. K. H.; Greenham, N. C.; Friend, R. H., Electroluminescence emission pattern of organic light-emitting diodes: Implications for device efficiency calculations. *Journal of Applied Physics* **2000,** *88* (2), 1073-1081.
45. Segal, M.; Baldo, M. A.; Holmes, R. J.; Forrest, S. R.; Soos, Z. G., Excitonic singlet-triplet ratios in molecular and polymeric organic materials. *Physical Review B* **2003,** *68* (7), 075211.
46. Setfos, User Manual, Version 5.2.
47. Adachi, C.; Baldo, M. A.; Thompson, M. E.; Forrest, S. R., Nearly 100% internal phosphorescence efficiency in an organic light-emitting device. *Journal of Applied Physics* **2001,** *90* (10), 5048-5051.
48. Kondakov, D. Y.; Pawlik, T. D.; Hatwar, T. K.; Spindler, J. P., Triplet annihilation exceeding spin statistical limit in highly efficient fluorescent organic light-emitting diodes. *Journal of Applied Physics* **2009,** *106* (12).
49. Bolink, H. J.; Coronado, E.; Costa, R. D.; Lardiés, N.; Ortí, E., Near-Quantitative Internal Quantum Efficiency in a Light-Emitting Electrochemical Cell. *Inorganic Chemistry* **2008,** *47* (20), 9149-9151.
50. Tsutsui, T., Progress in Electroluminescent Devices Using Molecular Thin Films. *MRS Bulletin* **1997,** *22* (6), 39-45.
51. Saxena, K.; Jain, V. K.; Mehta, D. S., A review on the light extraction techniques in organic electroluminescent devices. *Optical Materials* **2009,** *32* (1), 221-233.
52. Greenham, N. C.; Friend, R. H.; Bradley, D. D. C., Angular Dependence of the Emission from a Conjugated Polymer Light-Emitting Diode: Implications for efficiency calculations. *Advanced Materials* **1994,** *6* (6), 491-494.
53. Archer, E.; Hillebrandt, S.; Keum, C.; Murawski, C.; Murawski, J.; Tenopala-Carmona, F.; Gather, M. C., Accurate Efficiency Measurements of Organic Light-Emitting Diodes via Angle-Resolved Spectroscopy. *Advanced Optical Materials* **2021,** *9* (1), 2000838.
54. Shuai, Z.; Beljonne, D.; Silbey, R. J.; Brédas, J. L., Singlet and Triplet Exciton Formation Rates in Conjugated Polymer Light-Emitting Diodes. *Physical Review Letters* **2000,** *84* (1), 131-134.

55. Zhang, Y.; Forrest, S. R., Triplets Contribute to Both an Increase and Loss in Fluorescent Yield in Organic Light Emitting Diodes. *Physical Review Letters* **2012,** *108* (26), 267404.
56. Greenham, N. C.; Samuel, I. D. W.; Hayes, G. R.; Phillips, R. T.; Kessener, Y. A. R. R.; Moratti, S. C.; Holmes, A. B.; Friend, R. H., Measurement of absolute photoluminescence quantum efficiencies in conjugated polymers. *Chemical Physics Letters* **1995,** *241* (1), 89-96.
57. Brütting, W.; Frischeisen, J.; Schmidt, T. D.; Scholz, B. J.; Mayr, C., Device efficiency of organic light-emitting diodes: Progress by improved light outcoupling. *physica status solidi (a)* **2013,** *210* (1), 44-65.
58. Meerheim, R.; Furno, M.; Hofmann, S.; Lüssem, B.; Leo, K., Quantification of energy loss mechanisms in organic light-emitting diodes. *Applied Physics Letters* **2010,** *97* (25).
59. Furno, M.; Meerheim, R.; Hofmann, S.; Lüssem, B.; Leo, K., Efficiency and rate of spontaneous emission in organic electroluminescent devices. *Physical Review B* **2012,** *85* (11), 115205.
60. van Reenen, S.; Vitorino, M. V.; Meskers, S. C. J.; Janssen, R. A. J.; Kemerink, M., Photoluminescence quenching in films of conjugated polymers by electrochemical doping. *Physical Review B* **2014,** *89* (20), 205206.
61. Kirch, A. Charge-carrier dynamics in organic LEDs. Technische Universität Dresden, 2023.
62. Jen, T.-H.; Chen, S.-A., Singlet Exciton Fraction in Electroluminescence from Conjugated Polymer. *Scientific Reports* **2017,** *7* (1), 2889.
63. Iwasaki, Y.; Osasa, T.; Asahi, M.; Matsumura, M.; Sakaguchi, Y.; Suzuki, T., Fractions of singlet and triplet excitons generated in organic light-emitting devices based on a polyphenylenevinylene derivative. *Physical Review B* **2006,** *74* (19), 195209.
64. Wallikewitz, B. H.; Kabra, D.; Gélinas, S.; Friend, R. H., Triplet dynamics in fluorescent polymer light-emitting diodes. *Physical Review B* **2012,** *85* (4), 045209.
65. Shimotani, H.; Diguet, G.; Iwasa, Y., Direct comparison of field-effect and electrochemical doping in regioregular poly(3-hexylthiophene). *Applied Physics Letters* **2005,** *86* (2).
66. van Reenen, S.; Janssen, R. A. J.; Kemerink, M., Fundamental Tradeoff between Emission Intensity and Efficiency in Light-Emitting Electrochemical Cells. *Advanced Functional Materials* **2015,** *25* (20), 3066-3073.
67. Kim, S.-Y.; Kim, J.-J., Outcoupling efficiency of organic light emitting diodes and the effect of ITO thickness. *Organic Electronics* **2010,** *11* (6), 1010-1015.

68. Smith, L. H.; Wasey, J. A. E.; Barnes, W. L., Light outcoupling efficiency of top-emitting organic light-emitting diodes. *Applied Physics Letters* **2004,** *84* (16), 2986-2988.
69. Yamamoto, Y.; Slusher, R. E., Optical Processes in Microcavities. *Physics Today* **1993,** *46* (6), 66-73.
70. Liu, X.; Poitras, D.; Tao, Y.; Py, C., Microcavity organic light emitting diodes with double sided light emission of different colors. *Journal of Vacuum Science & Technology A* **2004,** *22* (3), 764-767.
71. Chin, A.; Chang, T. Y., Enhancement of quantum efficiency in thin photodiodes through absorptive resonance. *Journal of Lightwave Technology* **1991,** *9* (3), 321-328.
72. Dodabalapur, A.; Rothberg, L. J.; Jordan, R. H.; Miller, T. M.; Slusher, R. E.; Phillips, J. M., Physics and applications of organic microcavity light emitting diodes. *Journal of Applied Physics* **1996,** *80* (12), 6954-6964.
73. Deppe, D. G.; Lei, C.; Lin, C. C.; Huffaker, D. L., Spontaneous Emission from Planar Microstructures. *Journal of Modern Optics* **1994,** *41* (2), 325-344.
74. Perucco, B.; Reinke, N. A.; Rezzonico, D.; Moos, M.; Ruhstaller, B., Analysis of the emission profile in organic light-emitting devices. *Optics Express* **2010,** *18* (S2), A246-A260.
75. Markus, R., Characterization and Modelling of the Emission Zone and Exciton Dynamics in Doped Organic Light-Emitting Diodes. EPFL: 2019.
76. Lanz, T.; Lindh, E. M.; Edman, L., On the asymmetric evolution of the optical properties of a conjugated polymer during electrochemical p- and n-type doping. *Journal of Materials Chemistry C* **2017,** *5* (19), 4706-4715.
77. Ràfols-Ribé, J.; Zhang, X.; Larsen, C.; Lundberg, P.; Lindh, E. M.; Mai, C. T.; Mindemark, J.; Gracia-Espino, E.; Edman, L., Controlling the Emission Zone by Additives for Improved Light-Emitting Electrochemical Cells. *Advanced Materials* **2022,** *34* (8), 2107849.
78. Cort, J. W.; Kenji, M., Advantages of the mean absolute error (MAE) over the root mean square error (RMSE) in assessing average model performance. *Climate Research* **2005,** *30* (1), 79-82.
79. Barnes, W. L., Fluorescence near interfaces: The role of photonic mode density. *Journal of Modern Optics* **1998,** *45* (4), 661-699.
80. Zhang, X.; Ràfols-Ribé, J.; Mindemark, J.; Tang, S.; Lindh, M.; Gracia-Espino, E.; Larsen, C.; Edman, L., Efficiency Roll-Off in Light-Emitting Electrochemical Cells. *Advanced Materials* **2024,** *36* (15), 2310156.
81. Knapp, E.; Ruhstaller, B., Numerical analysis of steady-state and transient charge transport in organic semiconductor devices. *Optical and Quantum Electronics* **2011,** *42* (11), 667-677.

82. van der Holst, J. J. M.; van Oost, F. W. A.; Coehoorn, R.; Bobbert, P. A., Electron-hole recombination in disordered organic semiconductors: Validity of the Langevin formula. *Physical Review B* **2009,** *80* (23), 235202.
83. Rezzonico, D.; Perucco, B.; Knapp, E.; Haeusermann, R.; Reinke, N.; Müller, F.; Ruhstaller, B., Numerical analysis of exciton dynamics in organic light-emitting devices and solar cells. *Journal of Photonics for Energy* **2011,** *1* (1), 011005.
84. Tang, S.; Sandstrom, A.; Lundberg, P.; Lanz, T.; Larsen, C.; van Reenen, S.; Kemerink, M.; Edman, L., Design rules for light-emitting electrochemical cells delivering bright luminance at 27.5 percent external quantum efficiency. *Nature Communications* **2017,** *8* (1), 1190.
85. Wang, T.-W.; Su, H.-C., Extracting evolution of recombination zone position in sandwiched solid-state light-emitting electrochemical cells by employing microcavity effect. *Organic Electronics* **2013,** *14* (9), 2269-2277.
86. Sun, R.; Liao, C.-T.; Su, H.-C., Effects of incorporating salts with various alkyl chain lengths on carrier balance of light-emitting electrochemical cells. *Organic Electronics* **2014,** *15* (11), 2885-2892.
87. van Reenen, S.; Matyba, P.; Dzwilewski, A.; Janssen, R. A. J.; Edman, L.; Kemerink, M., Salt Concentration Effects in Planar Light-Emitting Electrochemical Cells. *Advanced Functional Materials* **2011,** *21* (10), 1795-1802.
88. Tordera, D.; Frey, J.; Vonlanthen, D.; Constable, E.; Pertegás, A.; Ortí, E.; Bolink, H. J.; Baranoff, E.; Nazeeruddin, M. K., Low Current Density Driving Leads to Efficient, Bright and Stable Green Electroluminescence. *Advanced Energy Materials* **2013,** *3* (10), 1338-1343.
89. Jenatsch, S.; Wang, L.; Leclaire, N.; Hack, E.; Steim, R.; Anantharaman, S. B.; Heier, J.; Ruhstaller, B.; Penninck, L.; Nüesch, F.; Hany, R., Visible light-emitting host-guest electrochemical cells using cyanine dyes. *Organic Electronics* **2017,** *48*, 77-84.
90. Lundberg, P.; Lindh, E. M.; Tang, S.; Edman, L., Toward Efficient and Metal-Free Emissive Devices: A Solution-Processed Host–Guest Light-Emitting Electrochemical Cell Featuring Thermally Activated Delayed Fluorescence. *ACS Applied Materials & Interfaces* **2017,** *9* (34), 28810-28816.
91. Lundberg, P.; Tsuchiya, Y.; Lindh, E. M.; Tang, S.; Adachi, C.; Edman, L., Thermally activated delayed fluorescence with 7% external quantum efficiency from a light-emitting electrochemical cell. *Nature Communications* **2019,** *10* (1), 5307.
92. Tang, S.; Lundberg, P.; Tsuchiya, Y.; Ràfols-Ribé, J.; Liu, Y.; Wang, J.; Adachi, C.; Edman, L., Efficient and Bright Blue Thermally

Activated Delayed Fluorescence from Light-Emitting Electrochemical Cells. *Advanced Functional Materials* **2022,** *32* (44), 2205967.
93. Baldo, M. A.; O'Brien, D. F.; You, Y.; Shoustikov, A.; Sibley, S.; Thompson, M. E.; Forrest, S. R., Highly efficient phosphorescent emission from organic electroluminescent devices. *Nature* **1998,** *395* (6698), 151-154.
94. Giebink, N. C.; D'Andrade, B. W.; Weaver, M. S.; Mackenzie, P. B.; Brown, J. J.; Thompson, M. E.; Forrest, S. R., Intrinsic luminance loss in phosphorescent small-molecule organic light emitting devices due to bimolecular annihilation reactions. *Journal of Applied Physics* **2008,** *103* (4).
95. Murawski, C.; Leo, K.; Gather, M. C., Efficiency roll-off in organic light-emitting diodes. *Advanced Materials* **2013,** *25* (47), 6801-27.
96. Wang, Y.; Zhu, Y.; Xie, G.; Zhan, H.; Yang, C.; Cheng, Y., Bright white electroluminescence from a single polymer containing a thermally activated delayed fluorescence unit and a solution-processed orange OLED approaching 20% external quantum efficiency. *Journal of Materials Chemistry C* **2017,** *5* (41), 10715-10720.
97. Rakhmanova, S. V.; Conwell, E. M., Mobility variation with field in conducting polymer films. *Synthetic Metals* **2001,** *116* (1), 389-391.
98. Amorim, C. A.; Cavallari, M. R.; Santos, G.; Fonseca, F. J.; Andrade, A. M.; Mergulhão, S., Determination of carrier mobility in MEH-PPV thin-films by stationary and transient current techniques. *Journal of Non-Crystalline Solids* **2012,** *358* (3), 484-491.
99. Gambino, S.; Bansal, A. K.; Samuel, I. D. W., Comparison of hole mobility in thick and thin films of a conjugated polymer. *Organic Electronics* **2010,** *11* (3), 467-471.
100. Jenatsch, S.; Regnat, M.; Hany, R.; Diethelm, M.; Nüesch, F.; Ruhstaller, B., Time-Dependent p–i–n Structure and Emission Zone in Sandwich-Type Light-Emitting Electrochemical Cells. *ACS Photonics* **2018,** *5* (4), 1591-1598.
101. Jenatsch, S.; Wang, L.; Bulloni, M.; Véron, A. C.; Ruhstaller, B.; Altazin, S.; Nüesch, F.; Hany, R., Doping Evolution and Junction Formation in Stacked Cyanine Dye Light-Emitting Electrochemical Cells. *ACS Applied Materials & Interfaces* **2016,** *8* (10), 6554-6562.
102. Meier, S. B.; Hartmann, D.; Winnacker, A.; Sarfert, W., The dynamic behavior of thin-film ionic transition metal complex-based light-emitting electrochemical cells. *Journal of Applied Physics* **2014,** *116* (10).
103. Matyba, P.; Yamaguchi, H.; Chhowalla, M.; Robinson, N. D.; Edman, L., Flexible and Metal-Free Light-Emitting Electrochemical Cells Based on Graphene and PEDOT-PSS as the Electrode Materials. *ACS Nano* **2011,** *5* (1), 574-580.

104. Kanagaraj, S.; Puthanveedu, A.; Choe, Y., Small Molecules in Light-Emitting Electrochemical Cells: Promising Light-Emitting Materials. *Advanced Functional Materials* **2020,** *30* (33), 1907126.
105. Johansson, T.; Mammo, W.; Andersson, M. R.; Inganäs, O., Light-Emitting Electrochemical Cells from Oligo(ethylene oxide)-Substituted Polythiophenes: Evidence for in Situ Doping. *Chemistry of Materials* **1999,** *11* (11), 3133-3139.
106. Hänisch, C.; Lenk, S.; Reineke, S., Refined Setup for Angle-Resolved Photoluminescence Spectroscopy of Thin Films. *Physical Review Applied* **2020,** *14* (6), 064036.